

# Holographic Entanglement Anisotropy as a Dark Deformation RG Probe in Hyperscaling-Violating $p$ -Wave Superfluids

Ji-Seong Chae<sup>†1</sup>

<sup>†</sup>*Department of Physics, Hanyang University, Seoul 04763, Korea*

## Abstract

We study dark-sector deformations of anisotropic  $p$ -wave superfluids in hyperscaling-violating black-brane backgrounds. The visible non-Abelian sector condenses a vector order parameter, breaks boundary spatial rotations, and supplies a directional entanglement probe. We use the strip-width dependence of holographic entanglement anisotropy to distinguish how hidden sectors enter the visible geometry. In four and five bulk dimensions, isotropic dark sources are projected out, hidden-current mixing gives a width-independent normalization of the visible anisotropic response, and a scalar gauge-kinetic portal produces a width-dependent signal through its radial Yang–Mills weight. Varying the hyperscaling-violation and dynamical exponents changes the radial weights, the visible normalization, and the scalar short-width power, but not the separation into null, scale-independent, and width-running channels. Thus the classification is not a peculiarity of one analytic background; it persists across the scaling geometries studied here. The three-dimensional case is treated separately as an interval response.

## I. INTRODUCTION

Gauge/gravity duality turns certain strongly coupled quantum systems into classical gravitational boundary-value problems. The original correspondence relates large- $N$  conformal gauge theories to gravity on asymptotically anti-de Sitter (AdS) spaces [1–4]. At finite temperature the simplest homogeneous saddle is a black brane, namely a planar black hole whose horizon extends along the boundary spatial directions and represents a thermal state of the boundary theory. The real-time prescription identifies infalling perturbations of this black brane with retarded correlators of boundary operators [5, 6]. Thus a bulk linear-response calculation can compute transport coefficients and order-parameter susceptibilities of the strongly coupled boundary theory. In weakly coupled systems the same quantities are often organized by quasiparticles: weakly damped excitations whose poles are sharp enough that they move for

---

<sup>1</sup> jiseongchae17@gmail.com

many microscopic times before losing phase information. Strong coupling removes this parametric separation between oscillation and damping; the relevant boundary correlator poles can be broad or absent, so a Boltzmann kinetic description built from long-lived carriers is not a controlled starting point. The black-brane perturbation problem therefore replaces a boundary quasiparticle kinetic theory rather than supplementing one.

A major lesson of the holographic transport program is that universal behavior is often tied to symmetry and channel structure. In isotropic Einstein gravity, transverse gravitons behave as minimally coupled massless fields, leading to the familiar shear-viscosity result  $\eta/s = 1/4\pi$  [7–9]. The membrane-paradigm derivation explains this universality as a horizon-coupling statement rather than a microscopic accident [6]. Fluid/gravity constructions then gave a systematic derivative-expansion interpretation of the same black-brane data [10, 11].

Anisotropic holographic superfluids are important precisely because they break this simple channel equivalence. In the non-Abelian  $p$ -wave construction, a temporal SU(2) gauge component sources a chemical potential, while a spatial component condenses along one chosen boundary spatial axis, which we call  $x_1$  [12, 13]. The phrase “selects a boundary direction” therefore means spontaneous breaking of boundary rotations, not the appearance or motion of a boundary. The condensate is dual to a vector current expectation value, schematically  $\langle J_{x_1}^1 \rangle$ , so the ordered phase breaks both the visible SU(2) flavor symmetry and spatial rotational symmetry. In such a phase, perturbations parallel and transverse to the ordered direction need not probe the same effective coupling. This mechanism underlies the non-universal shear response of anisotropic holographic superfluids [14–16]. Related  $p$ -wave and flavor-brane constructions, including backreacted and imbalanced variants, provide concrete checks: they exhibit source-free vector solutions, mean-field condensate scaling near  $\mu_c$ , and grand-potential comparisons between normal and ordered phases [59, 64, 65, 73, 74]. In models with competing condensates, the normal phase can first develop a linear zero mode at one value of the chemical potential while the thermodynamically preferred nonlinear solution family is selected elsewhere; this zero-mode point is the value at which the normal-phase Sturm–Liouville operator acquires a normalizable solution with vanishing source [60–62]. Reviews of holographic superconductivity and condensed-matter applications summarize this order-parameter dictionary [63, 66, 67]. It also motivates using anisotropic observables, rather than only scalar thermodynamic quantities, to detect hidden-sector imprints.

The dark-sector motivation comes from kinetic mixing and portal interactions. Hidden gauge sectors are generic in many extensions of the Standard Model, and Abelian kinetic mixing gives a simple low-energy portal between visible and hidden currents [17–21]. Holographic superconductors with dark matter sectors showed that such mixing can shift critical data, magnetic response, vortices, condensate flow and entanglement entropy [22–29]. Separately, visible-sector studies of anisotropic  $p$ -wave superfluids showed that the orientation difference of holographic entanglement entropy is a natural order-parameter diagnostic for the vector condensate [30]. We use that visible-sector construction as the reference observable, but ask a

different question: how hidden deformations appear, or fail to appear, in the same directional response. In phase-sensitive devices, such as holographic superconducting quantum interference devices (SQUIDs), a small hidden-sector coupling can become visible because the measured quantity is a difference or interference signal rather than a large absolute condensate amplitude [31]. In two-current Dirac-fluid models, the same idea appears as a hidden charge channel in the transport matrix [32, 33].

In the present work, we investigate the dark-sector deformation of the anisotropic superfluid in the hyperscaling-violation geometry. In that setting, the hidden sector is not merely an extra charge reservoir: once the  $p$ -wave condensate breaks rotations, the hidden sector couples differently to fluctuation channels aligned with and transverse to the order parameter [34]. This is why an anisotropic background is advantageous. A dark deformation that would look like a mild rescaling in an isotropic phase can become a directional source for holographic entanglement entropy ( $S_{\parallel}$ ,  $S_{\perp}$ ), shear response, or the vector-order condensate.

The remaining question is why the analysis should be extended beyond asymptotically AdS backgrounds. Asymptotic AdS corresponds to a relativistic ultraviolet (UV) fixed point, but many strongly correlated systems are better described over intermediate scales by non-relativistic scaling with a dynamical critical exponent  $z$  and a hyperscaling-violation exponent  $\theta$ . In this paper  $z$  controls the relative scaling of time and space, while  $\theta$  shifts the effective spatial dimensionality appearing in thermodynamics and entanglement. Hyperscaling-violating (HSV) geometries arise naturally in Einstein–Maxwell–dilaton effective theories and provide candidate gravity descriptions of scale-covariant finite-temperature and finite-density systems [35–38, 68–72]. The log-violating Huijse–Sachdev–Swingle (HSS) region corresponds to the opposite sign convention for the hyperscaling exponent and lies outside the  $\theta \geq 0$  scan used here; it is cited only as motivation for scale-sensitive entanglement probes. The HSV black brane is therefore an effective bulk dual for a boundary theory characterized by finite density, non-relativistic scaling and an effective spatial dimensionality shifted by  $\theta$ .

The field-theory dictionary in this effective HSV background is concrete enough for the purpose of this work. The Abelian field supporting charge density is dual to a conserved boundary current and its chemical potential. The visible  $SU(2)$  Yang-Mills field is dual to a global flavor current multiplet  $J_{\mu}^a$ . The temporal visible component sources the third flavor charge, while the spatial component  $B_{x_1}^1$  gives the vector condensate  $\langle J_{x_1}^1 \rangle$ . A hidden  $U(1)$  or hidden  $SU(2)$  gauge field is therefore interpreted as a hidden conserved current sector. A kinetic-mixing term in the bulk implements a current-current portal between visible and hidden sectors. A scalar or gauge-kinetic portal implements a scale-dependent deformation of the visible current kinetic operator, or equivalently a deformation of the radial weights controlling the visible current correlator.

This interpretation also clarifies what the HSV family contributes to the present question. Besides giving a mesoscopic radial picture of how an RT surface weights the bulk, the HSV backgrounds let us change the radial weights of the same anisotropic observable by varying  $\theta$ ,

$z$ , and  $D$ . The scan therefore asks two questions at once: which hidden-sector tensor structures are visible in  $S_{\perp} - S_{\parallel}$ , and which parts of that answer persist when the geometry is moved away from a single AdS reference point. In the results below, the answer is largely controlled by the hidden-sector channel rather than by a special value of  $(\theta, z)$ . The exponents change the visible normalization, the RT kernel, and the scalar UV power, but the null channels, the scale-independent hidden-current channel, and the width-running scalar kinetic channel remain separated. Recent work on anisotropic holographic superfluids in asymptotically HSV geometries provides the visible-sector analytic baseline we deform here [39]. More broadly, recent reconstruction and entanglement studies beyond asymptotic AdS emphasize that non-AdS scaling geometries can encode physically meaningful boundary response over finite radial or energy windows [40–42].

Entanglement entropy is a natural observable for this program because it is sensitive to geometry and orientation. The Ryu-Takayanagi prescription converts a boundary subregion into a bulk extremal area [43, 44]. Shape dependence, extrinsic geometry and first-law variations provide a controlled way to diagnose small metric deformations [45–52]. In the anisotropic phase we therefore compare interval entropy in  $D = 3$  and strip/slab entropies in  $D = 4, 5$ , especially the difference between orientations parallel and transverse to the vector condensate. This use of directional observables is consistent with the broader lesson from anisotropic holographic plasmas that different spatial channels need not share a universal effective coupling [75, 76].

The central observation of this paper is not that  $S_{\perp} - S_{\parallel}$  detects the visible vector order by itself; that is the visible-sector baseline. The new use is to compare hidden deformations against this calibrated anisotropic response. A scalar thermodynamic quantity can detect that a critical scale has shifted, but it cannot tell whether the hidden sector acts as a scale-independent current normalization or as a radial, scale-dependent deformation of the current operator. The orientation difference  $S_{\perp} - S_{\parallel}$ , viewed as a function of strip width, can do this. If the dark sector multiplies the anisotropic source by a constant, the ratio to the visible answer is independent of width. If the dark sector changes the radial weight of the Yang–Mills operator, the ratio runs with width. Thus the  $p$ -wave order supplies a direction and the RT strip supplies an energy-scale probe. The combined observable becomes a dark-sector renormalization-group (RG) diagnostic rather than just another shifted response coefficient.

We keep the visible  $p$ -wave system fixed and add hidden sectors to it. Thus the actions considered below should be read as

$$S_{\text{tot}}^{(i)} = S_{\text{bg}} + S_{\text{vis}} + \Delta S_{\text{dark}}^{(i)}, \quad (\text{I.1})$$

not as replacements for the visible Yang–Mills theory. The label  $i$  enumerates the dark cases;  $S_{\text{bg}}$  is the Einstein–Maxwell–dilaton background action,  $S_{\text{vis}}$  is the visible SU(2) Yang–Mills action, and  $\Delta S_{\text{dark}}^{(i)}$  is the corresponding hidden-sector deformation. We use a dimensionless radial coordinate  $u$ , with horizon at  $u = 1$  and boundary at  $u \rightarrow \infty$ . The visible ansatz is

$$B^a \tau^a = b(u) \tau^3 dt + \omega(u) \tau^1 dx_1, \quad (\text{I.2})$$

where  $B_M^a$  is the visible SU(2) gauge field and  $\tau^a$  are the generators. The temporal component  $b(u)$  fixes the grand-canonical source,  $b(u \rightarrow \infty) = \sqrt{3}\mu$ , with regularity condition  $b(1) = 0$  at the horizon. The spatial solution  $\omega(u)$  is dual to the  $p$ -wave vector order parameter. A source-free ordered solution is obtained by solving the coupled Euler–Lagrange equations for  $b$  and  $\omega$  with the non-normalizable part of  $\omega$  set to zero. The Sturm–Liouville problem is introduced only after this step, by linearising the same equations as  $\omega(u) = \epsilon\psi(u) + O(\epsilon^3)$ , where  $\epsilon$  is a small amplitude and  $\psi(u)$  is the normalized zero-mode solution.

This ordering is important for the present paper. A dark deformation can change the temporal equation for  $b$ , the spatial equation for  $\omega$ , or both. Therefore we first derive the radial equations of motion for the visible problem and then repeat the derivation after each hidden-sector term is added. Only afterwards do we extract the critical chemical potential from the linearized equation and compare the ordered-state grand potentials. This follows the standard logic of holographic superconductors and anisotropic superfluids: model and ansatz, radial equations, numerical solutions for  $b$  and  $\omega$ , critical point, and finally free-energy or entanglement checks [15, 39, 53–58].

The hidden-sector deformations studied here fall into three classes. Case I contains temporal hidden gauge fields. Case II is a hidden-SU(2) kinetic-mixing system; without an independent hidden chemical potential it remains analytically tractable because the visible and hidden spatial vector solutions share one radial shape with a constant mixing ratio. Case III adds a hidden dark singlet scalar  $\Phi$ , dual to a dark scalar boundary operator  $\mathcal{O}_\Phi$ , coupled to the visible sector only through a portal. A mass portal  $\lambda_{\Phi B}\Phi^2 B^2$  (Case III-a) adds an isotropic cost that raises the critical chemical potential. A kinetic portal  $Z_{\text{dm}}(\Phi)G^2$  (Case III-b) instead changes both the normal-phase temporal component and the spatial vector zero mode. Its critical-point shift is therefore background dependent rather than a universal lowering or raising. These dark-scalar portals are used as representative settings for the competition between an isotropic scalar channel, the anisotropic  $p$ -wave channel, and coexistence.

The visible SU(2) problem has an analytic reference sector,  $d(1 + \theta) = 3$  and  $z = 1$ , where  $d = D - 2$  is the number of boundary spatial directions. This reference sector contains the AdS<sub>5</sub> point  $(D, \theta, z) = (5, 0, 1)$  and the HSV analytic points  $(4, 1/2, 1)$  and  $(3, 2, 1)$ . We use it only to normalize the visible  $p$ -wave solution and to check the coupled hidden-current law. The main numerical survey then varies the geometry: for each displayed dimension we scan representative regions of the null-energy-condition (NEC) allowed  $(\theta, z)$  domain and compare every dark case with the visible SU(2) answer. The scan is not meant to find a sharply tuned HSV point. It tests how much of the entanglement classification is controlled by the radial scaling exponents and how much is controlled by the tensor structure of the hidden deformation. When a figure shows only a slice, such as the  $z = 2$  slice in Fig. 1, the complementary dependence is shown in Fig. 2 or is algebraically absent, as in the Case-II ratios. We do not claim a fully backreacted global phase diagram over the whole  $(D, \theta, z)$  space.

The organization is as follows. Section II fixes the radial coordinate and derives the visible

and dark-deformed equations of motion for  $b$  and  $\omega$ . Section III reviews the visible HSV critical point and gives a general operator-level account of dark response; the hidden-SU(2) coupled-mode law is treated there only as one solvable model. Section IV defines the HEE observables, the null-channel source rules, and the gauge-kinetic-portal susceptibility as a linear-response coefficient before explaining the first-law and condensate checks. Section V then presents the results in the order dictated by the physics: the strip-difference selection rule, the gauge-kinetic-portal susceptibility and its short-distance decoupling, the HSV-dependent critical-scale shift, and the radial-solution mechanism. Section VI summarizes the scope of the result, and Appendix A collects supporting plots.

## II. MODEL AND EQUATIONS OF MOTION

This section fixes the undeformed holographic model before any hidden sector is added. We first write the complete Einstein–dilaton– $U(1)$ –SU(2) action and its Euler–Lagrange equations. We then insert the HSV black-brane background and the visible  $p$ -wave ansatz. The dark sectors are introduced only afterwards, as deformations of the same Yang–Mills equations. This order is important: the critical-point problem is not postulated as a Sturm–Liouville equation; it is obtained by linearising the explicit radial Yang–Mills equations around the isotropic normal phase.

### II.A. Visible sector: Anisotropic holographic superfluid

The undeformed theory on which all dark-sector cases are built is

$$S_0 = \frac{1}{\kappa_D^2} \int d^D x \sqrt{-g} \left[ R - \frac{1}{2} g^{MN} \partial_M \phi \partial_N \phi + V_0 e^{\gamma \phi} - \frac{\kappa_D^2}{4g_U^2} e^{\lambda_U \phi} F_{MN} F^{MN} - \frac{\kappa_D^2}{4g_{\text{YM}}^2} e^{\lambda_{\text{YM}} \phi} G_{MN}^a G^{aMN} \right], \quad (\text{II.1})$$

where  $D = d + 2$ ,  $M, N = 0, \dots, D - 1$ , and  $d$  is the number of boundary spatial directions. We use

$$\delta \equiv \frac{\kappa_D}{g_{\text{YM}}} \quad (\text{II.2})$$

as the Yang–Mills backreaction-strength parameter. Thus the leading metric response sourced by the vector condensate is of order  $\delta^2 \epsilon^2$ . In the probe Yang–Mills critical-mode calculation  $\delta$  is only a bookkeeping parameter, while in the RT first-variation calculation it multiplies the first non-trivial Einstein response. The Abelian and non-Abelian field strengths are

$$F_{MN} = \partial_M A_N - \partial_N A_M, \quad G_{MN}^a = \partial_M B_N^a - \partial_N B_M^a - \epsilon^{abc} B_M^b B_N^c, \quad (\text{II.3})$$

with  $B = B_M^a \tau^a dx^M$ ,  $[\tau^a, \tau^b] = i \epsilon^{abc} \tau^c$ , and  $\text{Tr}(\tau^a \tau^b) = \delta^{ab}/2$ .

Varying (II.1) gives four sets of bulk equations. The scalar equation is

$$\mathcal{X} \equiv \frac{1}{\sqrt{-g}} \partial_M (\sqrt{-g} g^{MN} \partial_N \phi) + \gamma V_0 e^{\gamma\phi} - \frac{\kappa_D^2 \lambda_U}{4g_U^2} e^{\lambda_U \phi} F_{MN} F^{MN} - \frac{\kappa_D^2 \lambda_{\text{YM}}}{4g_{\text{YM}}^2} e^{\lambda_{\text{YM}} \phi} G_{MN}^a G^{aMN} = 0. \quad (\text{II.4})$$

The Maxwell equation is

$$\mathcal{Y}_U^N \equiv \frac{1}{\sqrt{-g}} \partial_M (\sqrt{-g} e^{\lambda_U \phi} F^{MN}) = 0, \quad (\text{II.5})$$

and the visible Yang–Mills equation is

$$\mathcal{Y}_{\text{YM}}^{aN} \equiv \frac{1}{\sqrt{-g}} \partial_M (\sqrt{-g} e^{\lambda_{\text{YM}} \phi} G^{aMN}) + e^{\lambda_{\text{YM}} \phi} \epsilon^{abc} G^{bMN} B_M^c = 0. \quad (\text{II.6})$$

Finally, the trace-reversed Einstein equation is

$$\begin{aligned} \mathcal{W}_{MN} \equiv & R_{MN} - \frac{1}{2} \partial_M \phi \partial_N \phi + \frac{1}{D-2} V_0 e^{\gamma\phi} g_{MN} \\ & - \frac{\kappa_D^2}{2g_U^2} e^{\lambda_U \phi} \left( F_{MP} F_N^P - \frac{1}{2(D-2)} g_{MN} F_{PQ} F^{PQ} \right) \\ & - \frac{\kappa_D^2}{2g_{\text{YM}}^2} e^{\lambda_{\text{YM}} \phi} \left( G_{MP}^a G_N^a{}^P - \frac{1}{2(D-2)} g_{MN} G_{PQ}^a G^{aPQ} \right) = 0. \end{aligned} \quad (\text{II.7})$$

Equations (II.4)–(II.7) are the original equations before any dark-sector deformation is introduced.

The isotropic HSV black-brane seed is obtained from the ansatz

$$ds^2 = r_h^{2\theta} u^{2\theta} \left[ -u^{2z} f(u) dt^2 + \frac{du^2}{u^2 f(u)} + u^2 \delta_{ij} dx^i dx^j \right], \quad u \equiv \frac{r}{r_h}, \quad (\text{II.8})$$

with horizon  $u = 1$ , boundary  $u \rightarrow \infty$ , and

$$f(u) = 1 - u^{-n_h}, \quad n_h = d\theta + z + d. \quad (\text{II.9})$$

The dilaton solution and the EMD couplings are fixed by the HSV equations:

$$\phi(u) = \phi_0 + \sqrt{2d(1+\theta)(\theta+z-1)} \ln u, \quad (\text{II.10})$$

$$\lambda_{\text{YM}} = \sqrt{\frac{2(\theta+z-1)}{d(1+\theta)}}, \quad \gamma = -\frac{2\theta}{\sqrt{2d(1+\theta)(\theta+z-1)}}, \quad (\text{II.11})$$

$$\lambda_U = -\frac{2\theta(d-1) + 2d}{\sqrt{2d(1+\theta)(\theta+z-1)}}, \quad V_0 = e^{-\gamma\phi_0} (d\theta + z + d - 1)(d\theta + z + d). \quad (\text{II.12})$$

In the probe computations below the background SU(2) charge term in  $f(u)$  is dropped by taking  $\kappa_D^2/g_{\text{YM}}^2 \rightarrow 0$ ; the visible Yang–Mills fields are then solved on the fixed HSV geometry.

The null-energy condition is not an additional numerical assumption. It is the algebraic condition obtained by contracting the Einstein equation with independent null vectors of the HSV metric. Let

$$k_{(1)}^M = (\sqrt{g^{uu}}, \sqrt{-g^{tt}}, 0, \dots, 0), \quad k_{(2)}^M = (0, \sqrt{-g^{tt}}, \sqrt{g^{x_1 x_1}}, 0, \dots, 0), \quad (\text{II.13})$$

which satisfy  $g_{MN}k_{(i)}^M k_{(i)}^N = 0$ . Since the potential term is proportional to  $g_{MN}$ , it drops out after contraction with a null vector. Using (II.7), the two independent NEC contractions reduce to the Ricci differences

$$T_{MN}k_{(1)}^M k_{(1)}^N \geq 0 \iff R^u_u - R^t_t = d(1+\theta)(\theta+z-1)u^{-2\theta}f(u) \geq 0, \quad (\text{II.14})$$

$$T_{MN}k_{(2)}^M k_{(2)}^N \geq 0 \iff R^{x_1}_{x_1} - R^t_t = (z-1)[z+d(1+\theta)]u^{-2\theta} \geq 0. \quad (\text{II.15})$$

Outside the horizon  $f(u) > 0$ . Thus the allowed HSV domain is

$$(1+\theta)(\theta+z-1) \geq 0, \quad (z-1)[z+d(1+\theta)] \geq 0. \quad (\text{II.16})$$

The surveys in this paper use  $z \geq 1$  and  $\theta \geq 0$ , so both inequalities are automatically satisfied; points outside (II.16) are not used in the numerical scans.

The inverse metric components entering the Yang–Mills radial reduction are

$$g^{uu} = r_h^{-2\theta} u^{-2\theta} u^2 f(u), \quad g^{tt} = -r_h^{-2\theta} u^{-2\theta} u^{-2z} f(u)^{-1}, \quad g^{x_i x_i} = r_h^{-2\theta} u^{-2\theta} u^{-2}. \quad (\text{II.17})$$

The overall powers of  $r_h$  set dimensions and will be suppressed in the dimensionless radial equations below.

## II.B. Visible SU(2) Yang–Mills sector

The visible gauge field is an SU(2) connection  $B = B_M^a \tau^a dx^M$  with field strength

$$G_{MN}^a = \partial_M B_N^a - \partial_N B_M^a - \epsilon^{abc} B_M^b B_N^c, \quad (\text{II.18})$$

and the Yang–Mills action is

$$S_{\text{vis}} = -\frac{1}{4g_{\text{YM}}^2} \int d^{d+2}x \sqrt{-g} e^{\lambda_{\text{YM}}\phi} G_{MN}^a G^{aMN}. \quad (\text{II.19})$$

The  $p$ -wave ansatz is

$$B^a \tau^a = b(u) \tau^3 dt + \omega(u) \tau^1 dx_1. \quad (\text{II.20})$$

Substituting (II.20) into (II.18), the non-vanishing radial field-strength components are

$$G_{ut}^3 = b'(u), \quad G_{ux_1}^1 = \omega'(u), \quad G_{tx_1}^2 = -b(u)\omega(u), \quad (\text{II.21})$$

where a prime denotes  $d/du$ . Contracting with the inverse metric gives a one-dimensional radial functional. It is useful not to quote the determinant alone, because the only invariant

data entering the fluctuation problem are the products  $\sqrt{-g} e^{\lambda_{\text{YM}}\phi} g^{MM} g^{NN}$ . In the radial gauge and normalisation used throughout the numerical evidence pack, these products are fixed by the HSV background and reduce to the weights displayed below. The radial Yang–Mills functional, expanded to quadratic order in the spatial mode  $\omega$ , is

$$\mathcal{L}_{\text{YM}}^{(1d)} = -\frac{1}{2} [\mathcal{P}_b(u) b'^2 + \mathcal{P}_\omega(u) \omega'^2 - \mathcal{M}(u) b^2 \omega^2], \quad (\text{II.22})$$

where we define, up to an overall positive constant independent of  $u$ ,

$$\mathcal{P}_b(u) \equiv \sqrt{-g} e^{\lambda_{\text{YM}}\phi} (-g^{uu}) (-g^{tt}) = u^{d(1+\theta)+z-1}, \quad (\text{II.23})$$

$$\mathcal{P}_\omega(u) \equiv \sqrt{-g} e^{\lambda_{\text{YM}}\phi} g^{uu} g^{x_1 x_1} = u^{n_p} f(u), \quad n_p \equiv d\theta + d + 3z - 3, \quad (\text{II.24})$$

$$\mathcal{M}(u) \equiv \sqrt{-g} e^{\lambda_{\text{YM}}\phi} (-g^{tt}) g^{x_1 x_1} = \frac{u^{n_h-5}}{f(u)}. \quad (\text{II.25})$$

Equations (II.23)–(II.25) are the explicit radial reduction used in the eigenvalue problem. For example,  $\mathcal{P}_\omega$  is the coefficient of the spatial gauge kinetic term  $G_{u x_1}^1 G^{1 u x_1}$ ; after inserting the HSV solution and the dilaton coupling, the power of  $u$  is  $n_p = d\theta + d + 3z - 3$ , while the horizon zero comes entirely from the factor  $g^{uu} \propto f$ . The electric weight  $\mathcal{M}$  instead contains  $(-g^{tt}) \propto f^{-1}$ , which is why it carries the reciprocal horizon factor.

The Euler–Lagrange equations obtained from varying  $b$  and  $\omega$  in the one-dimensional action  $I_{\text{YM}}^{(1d)} = \int du \mathcal{L}_{\text{YM}}^{(1d)}$  are

$$\partial_u(\mathcal{P}_b b') - \mathcal{M} b \omega^2 = 0, \quad (\text{II.26})$$

$$\partial_u(\mathcal{P}_\omega \omega') + \mathcal{M} b^2 \omega = 0. \quad (\text{II.27})$$

Equations (II.26) and (II.27) are the equations solved for the radial fields. In a numerical shooting or boundary-value formulation one imposes regular horizon data

$$b(1) = 0, \quad \omega(1) = \omega_h, \quad (\text{II.28})$$

with the first derivatives fixed by the regular near-horizon expansion. At the boundary the grand-canonical ensemble fixes

$$b(u) = \sqrt{3} \mu - \rho_b u^{-(n_h-2)} + \dots, \quad \omega(u) = \omega_{\text{src}} + \omega_{\text{vev}} u^{-(n_p-1)} + \dots, \quad (\text{II.29})$$

where the source-free  $p$ -wave solution has  $\omega_{\text{src}} = 0$  and  $\omega_{\text{vev}} \propto \langle J_{x_1}^1 \rangle$ . Thus the functions  $b(u)$  and  $\omega(u)$  are obtained directly from the Euler–Lagrange equations. The Sturm–Liouville method enters only after expanding these same equations around the isotropic solution.

Near the linearised critical point we write

$$b(u) = b_0(u) + O(\epsilon^2), \quad \omega(u) = \epsilon \psi(u) + O(\epsilon^3), \quad (\text{II.30})$$

where  $b_0$  is the source-free isotropic temporal component

$$b_0(u) = \sqrt{3} \mu (1 - u^{-(n_h-2)}), \quad (\text{II.31})$$

satisfying  $b_0(1) = 0$  and  $b_0(u) \rightarrow \sqrt{3}\mu$  as  $u \rightarrow \infty$ . At leading order,  $\psi$  obeys the Sturm–Liouville equation

$$\partial_u[P(u)\psi'(u)] + Q(u;\mu)\psi(u) = 0, \quad (\text{II.32})$$

with

$$P(u) = u^{n_p}(1 - u^{-n_h}), \quad Q(u;\mu) = 3\mu^2 \frac{u^{n_h-5}(1 - u^{-(n_h-2)})^2}{1 - u^{-n_h}}. \quad (\text{II.33})$$

The critical chemical potential  $\mu_c(d, z, \theta)$  is the smallest  $\mu$  for which (II.32) has a normalizable solution with vanishing source at  $u \rightarrow \infty$ . At the analytic reference point  $d(1 + \theta) = 3$ ,  $z = 1$ , one has  $n_h = 4$ ,  $n_p = 3$ , and the closed-form zero mode

$$\psi_0(u) = \frac{u^2}{(1 + u^2)^2}, \quad \mu_c = \frac{4}{\sqrt{3}}. \quad (\text{II.34})$$

### 1. Thermodynamic meaning of the reference transition

The normal phase has  $\omega = 0$  and is spatially isotropic. A source-free normalizable solution of Eq. (II.32) is the linear critical point of the  $p$ -wave ordered phase; in the boundary theory this is the transition to a phase with vector order parameter  $\langle J_{x_1}^1 \rangle \neq 0$ . We use the grand-potential criterion of Park–Park–Oh: if

$$\Delta\Omega \equiv \Omega_{\omega \neq 0} - \Omega_{\omega=0} < 0, \quad (\text{II.35})$$

then the anisotropic phase is thermodynamically favoured at the same boundary chemical potential.

The perturbative near-critical expansion is most transparent in the inverse radial coordinate  $\xi = 1/u$ . Let

$$\omega(\xi) = \epsilon \psi_1(\xi) + O(\epsilon^3), \quad b(\xi) = b_0(\xi) + \epsilon^2 \beta_2(\xi) + O(\epsilon^4), \quad (\text{II.36})$$

with  $\beta_2(0) = \beta_2(1) = 0$ . The order- $\epsilon^2$  temporal backreaction solves

$$\partial_\xi[K_b(\xi)\partial_\xi\beta_2] = M(\xi)b_0(\xi)\psi_1^2(\xi), \quad K_b(\xi) = \xi^{3-d-d\theta-z} = \xi^{-(n_h-3)}. \quad (\text{II.37})$$

For the source-free solution comparison at the same boundary chemical potential,

$$\Delta\Omega_{A|N} = -\epsilon^4 \int_0^1 d\xi K_b(\xi)(\partial_\xi\beta_2)^2 + O(\epsilon^6) < 0, \quad (\text{II.38})$$

whenever the local solution family exists. This is the reference thermodynamic sign used below, following the Park–Park–Oh probe free-energy criterion [58]. It should not be confused with a finite-amplitude attempt to draw a pure-visible ordered–ordered boundary  $z_*(\theta)$ . The controlled dark-sector observable in this paper is the critical surface  $\mu_c$  and the associated near-critical energetics.

Every dark-sector deformation below modifies (II.32); the key question is whether the modification changes only the eigenvalue  $\mu_c$  or also the structure of the operator.

## II.C. General dark-sector deformations of the Yang–Mills equations

We now add dark sectors to the same undeformed action (II.1). The bookkeeping is

$$S_{\text{tot}}^{(i)} = S_0 + \Delta S_{\text{dark}}^{(i)}, \quad (\text{II.39})$$

where  $S_0$  already contains the visible SU(2) field  $B_M^a$ . The cases below differ only in the additional term  $\Delta S_{\text{dark}}^{(i)}$ . In each case we display the deformation of the same two visible radial equations,

$$\partial_u(\mathcal{P}_b b') - \mathcal{M} b \omega^2 = 0, \quad \partial_u(\mathcal{P}_\omega \omega') + \mathcal{M} b^2 \omega = 0, \quad (\text{II.40})$$

rather than introducing a new critical equation by hand. Schematically, a general dark deformation changes these equations to

$$\partial_u(\mathcal{P}_b^{\text{eff}} b' + \mathcal{P}_{bX}^{\text{eff}} X') - \mathcal{M}_{\text{eff}} b \omega^2 + \dots = 0, \quad (\text{II.41})$$

$$\partial_u(\mathcal{P}_\omega^{\text{eff}} \omega') + \mathcal{Q}_{\text{eff}}(u; b, X, \Phi) \omega = 0. \quad (\text{II.42})$$

The dots denote possible scalar or hidden-gauge source terms. The linear critical problem is obtained from (II.42) by setting  $b = b_0 + O(\omega^2)$  and keeping the term linear in  $\omega$ . The nonlinear solution family and the grand potential require the full radial system.

*a. Radial equations for the dark sectors.* For clarity we collect the radial equations that are analytically reduced or integrated numerically. The derivation is always the same: insert the ansatz into the component field strengths, contract with the HSV metric, write the one-dimensional action, and vary with respect to the radial fields. The visible reference pair is Eq. (II.40). Case I adds the hidden Abelian temporal component  $x(u)$ , giving

$$\partial_u[\mathcal{P}_b b' + \chi \mathcal{P}_m x'] - \mathcal{M} b \omega^2 = 0, \quad (\text{II.43})$$

$$\partial_u[\mathcal{P}_X x' + \chi \mathcal{P}_m b'] = 0, \quad (\text{II.44})$$

$$\partial_u(\mathcal{P}_\omega \omega') + \mathcal{M} b^2 \omega = 0. \quad (\text{II.45})$$

On the normal phase these equations are analytically reduced by the two first integrals for  $b'$  and  $x'$ ; the remaining zero-mode equation is the visible Sturm–Liouville problem with the corresponding normal-phase electric solution inserted. Because  $x(u)$  is a temporal Abelian field, no anisotropic spatial source is created at this order.

Case II keeps both visible and hidden non-Abelian spatial components,  $B_{x_1}^1 = \omega_v(u)$  and  $C_{x_1}^1 = \omega_d(u)$ , together with temporal components  $b(u)$  and  $\eta(u)$ . To quadratic order in the spatial modes the component equations are

$$\partial_u \left[ \mathcal{P}_b \left( b' + \frac{\alpha_{\text{dm}}}{2} \eta' \right) \right] - \mathcal{M} \left( b \omega_v^2 + \frac{\alpha_{\text{dm}}}{2} \eta \omega_v \omega_d \right) = 0, \quad (\text{II.46})$$

$$\partial_u \left[ \mathcal{P}_b \left( \eta' + \frac{\alpha_{\text{dm}}}{2} b' \right) \right] - \mathcal{M} \left( \eta \omega_d^2 + \frac{\alpha_{\text{dm}}}{2} b \omega_v \omega_d \right) = 0, \quad (\text{II.47})$$

$$\partial_u \left[ \mathcal{P}_\omega \left( \omega'_v + \frac{\alpha_{\text{dm}}}{2} \omega'_d \right) \right] + \mathcal{M} \left( b^2 \omega_v + \frac{\alpha_{\text{dm}}}{2} b \eta \omega_d \right) = 0, \quad (\text{II.48})$$

$$\partial_u \left[ \mathcal{P}_\omega \left( \omega'_d + \frac{\alpha_{\text{dm}}}{2} \omega'_v \right) \right] + \mathcal{M} \left( \eta^2 \omega_d + \frac{\alpha_{\text{dm}}}{2} b \eta \omega_v \right) = 0. \quad (\text{II.49})$$

The normal-phase equations integrate once, as in Eq. (II.67). In the minimal ensemble the constant-ratio ansatz  $\omega_d = \gamma \omega_v$  then reduces Eqs. (II.48) and (II.49) to the two-channel algebraic law in Eq. (III.11); no further numerical assumption is made in Fig. 3.

Case III-a uses the sourced scalar solution  $\Phi(u)$  from the covariant Klein–Gordon equation (II.80). The mass portal leaves the temporal equation unchanged and adds the scalar cost to the spatial equation,

$$\partial_u(\mathcal{P}_b b') - \mathcal{M} b \omega^2 = 0, \quad (\text{II.50})$$

$$\partial_u(\mathcal{P}_\omega \omega') + \mathcal{M} b^2 \omega - 2\alpha_{\text{dm}}^2 \lambda_{\Phi B} \sqrt{-g} g^{x_1 x_1} \Phi^2 \omega = 0, \quad (\text{II.51})$$

$$\partial_u(\sqrt{-g} g^{uu} \Phi') - \sqrt{-g} m_\Phi^2 e^{\lambda_{\Phi\phi} \phi} \Phi = 0. \quad (\text{II.52})$$

The scalar is rotationally isotropic, so this case is important for the critical scale but null in the leading strip-orientation difference.

Case III-b uses the same scalar BVP but places the scalar in the Yang–Mills kinetic matrix. Defining  $Z(u) = 1 + \lambda_Z \Phi(u)^2 + O(\lambda_Z^2)$ , with  $\lambda_Z$  the dimensionless scalar gauge-kinetic portal coefficient, the normal-phase electric solution is obtained analytically up to one quadrature,

$$b_Z(u) = b_\infty \frac{\int_1^u \frac{dv}{Z(v) \mathcal{P}_b(v)}}{\int_1^\infty \frac{dv}{Z(v) \mathcal{P}_b(v)}}. \quad (\text{II.53})$$

The spatial zero mode is then the self-adjoint equation

$$\partial_u[Z(u) \mathcal{P}_\omega(u) \psi'_Z(u)] + Z(u) \mathcal{M}(u) b_Z(u)^2 \psi_Z(u) = 0, \quad (\text{II.54})$$

with source-free UV boundary condition for  $\psi_Z$ . These equations define the Case-III-b radial problem and the corresponding traceless stress source written later in Eq. (IV.59). The dense scalar-portal scan shown in the figures uses the short-width expansion of this construction. After solving the scalar BVP, the displayed scan uses the leading short-width scaling derived in Sec. IV. The absolute coefficient is not interpreted, because it receives finite RT-moment and first-order field-correction contributions.

It is useful to distinguish the visible order parameter from the dark sector. The  $SU(2)$  Yang–Mills field  $B_M^a$  is the visible sector in our terminology:  $B_t^3 = b(u)$  defines the visible chemical potential and  $B_{x_1}^1 = \omega(u)$  is the vector order parameter responsible for the anisotropic phase. Cases I and II add hidden gauge fields: an Abelian field  $X_M$  and a second non-Abelian field  $C_M^a$ . Cases III-a and III-b add a hidden dark scalar  $\Phi$ , dual to a dark scalar operator  $\mathcal{O}_\Phi$ , which is neutral under the visible  $SU(2)$ . Neutral here means only that  $\Phi$  carries no visible flavor charge; it does *not* mean that the scalar is a visible-sector deformation. It is an independent dark-sector field, and its only communication with the visible  $p$ -wave system is through portal couplings.

We use  $\alpha_{\text{dm}}$  as the dark-sector portal strength throughout the paper, with the precise operator depending on the case. In the hidden-gauge cases it is the usual kinetic-mixing parameter. In the dark-scalar cases it multiplies the scalar portal,

$$\begin{aligned}\Delta S_{\text{dark}}^{\text{III-a}} &= - \int d^{d+2}x \sqrt{-g} \alpha_{\text{dm}}^2 \lambda_{\Phi B} \Phi^2 B_M^a B^{aM}, \\ Z_{\text{dm}}(\Phi) &= 1 + \lambda_Z \Phi^2 + O(\lambda_Z^2), \quad \lambda_Z = O(\alpha_{\text{dm}}^2).\end{aligned}\tag{II.55}$$

Thus the scalar cases remain dark-sector deformations in the same sense as the hidden gauge cases: a field outside the visible  $SU(2)$  order-parameter sector modifies the visible current operator through a controlled portal. In numerical plots of the dark-scalar portals, the scalar-source normalization is specified explicitly when the figures are discussed; no additional effective coupling is introduced.

The four deformations are chosen to span the minimal ways in which a dark sector outside the visible  $p$ -wave order parameter can affect the HSV superfluid.

- Case I represents the simplest hidden Abelian current sector. It tests whether an additional  $U(1)_X$  charge sector, coupled only through the dark portal and backreaction, can modify the visible critical point and geometric response without introducing a second vector order parameter.
- Case II represents a genuinely non-Abelian hidden sector. Since the hidden field  $C_M^a$  has the same adjoint structure as the visible  $SU(2)$  field  $B_M^a$ , this case gives the cleanest test of hidden non-Abelian kinetic mixing and leads to a closed two-channel eigenvalue law controlled by the visible–hidden mixing ratio  $\gamma(\alpha_{\text{dm}})$ .
- Case III-a is a hidden dark scalar with an  $\alpha_{\text{dm}}$ -controlled mass portal. Being isotropic, it tests whether a dark scalar environment that raises the visible-vector cost without selecting a spatial direction can affect the leading anisotropic HEE response.
- Case III-b is the kinetic portal of the same hidden dark scalar. The color-blind factor  $Z_{\text{dm}}(\Phi(u))$  reweights the visible current operator radially, so it shifts the critical point by a radially dependent amount and generates a non-null geometric response. It is the dark-scalar counterpart of hidden gauge mixing.

*b. Gauge structure of the deformations.* Cases I and II should be understood as hidden gauge sectors only after the residual gauge symmetry is specified. The Abelian mixing in Case I is written in the  $U(1)_3$  direction selected by the visible chemical potential and therefore assumes the normal-phase embedding that leaves a color-3 Abelian subgroup. The non-Abelian kinetic mixing in Case II is invariant under the diagonal subgroup of  $SU(2)_{\text{vis}} \times SU(2)_{\text{hid}}$ , rather than under two independent non-Abelian gauge rotations. Cases III-a and III-b are not hidden gauge sectors. They are scalar dark deformations: the former is treated as an isotropic scalar stress or effective cost term, while the latter is a gauge-kinetic scalar portal  $e^{\lambda_{\text{YM}}\phi} G^2 \rightarrow e^{\lambda_{\text{YM}}\phi} Z(\Phi) G^2$ .

Thus “dark” means external to the visible  $p$ -wave order-parameter sector, whereas “hidden gauge” is reserved for Cases I and II.

1. *Case I: temporal hidden  $U(1)$  gauge sector*

The simplest dark extension adds a hidden Abelian gauge field  $X_M$  with field strength

$$X_{MN} = \partial_M X_N - \partial_N X_M \quad (\text{II.56})$$

and a kinetic-mixing portal with the visible color-3 electric field:

$$\Delta S_X = -\frac{1}{4} \int d^D x \sqrt{-g} [Z_X(\phi) X_{MN} X^{MN} + 2\chi Z_m(\phi) G_{MN}^3 X^{MN}]. \quad (\text{II.57})$$

The full action is  $S_{\text{tot}}^{(X)} = S_0 + \Delta S_X$ . With the temporal ansatz

$$X = x(u)dt, \quad X_{ut} = x'(u), \quad (\text{II.58})$$

the radial electric weights are

$$\mathcal{P}_X(u) = \sqrt{-g} Z_X(\phi) (-g^{uu} g^{tt}), \quad \mathcal{P}_m(u) = \sqrt{-g} Z_m(\phi) (-g^{uu} g^{tt}). \quad (\text{II.59})$$

The temporal equations are no longer the undeformed visible equation  $\partial_u(\mathcal{P}_b b') - \mathcal{M}b\omega^2 = 0$ . They become

$$\partial_u[\mathcal{P}_b b' + \chi \mathcal{P}_m x'] - \mathcal{M}b\omega^2 = 0, \quad (\text{II.60})$$

$$\partial_u[\mathcal{P}_X x' + \chi \mathcal{P}_m b'] = 0. \quad (\text{II.61})$$

The spatial visible equation is still

$$\partial_u(\mathcal{P}_\omega \omega') + \mathcal{M}b^2\omega = 0. \quad (\text{II.62})$$

Thus Case I changes the temporal electric sector, and therefore the relation between the boundary chemical potentials and the radial field  $b(u)$ . It does *not* introduce a new direct mass term for  $\omega$  at the linear probe level. If the hidden Abelian field is kept probe and the HSV geometry is fixed, the source-free vector operator is the same as the visible one after the appropriate temporal solution  $b_0(u)$  has been chosen.

2. *Case II: hidden  $SU(2)$  with kinetic mixing*

*a. Corrected Case-II coupled mode.* Case II is a coupled-current problem. The visible and hidden spatial modes must be diagonalized together. Equation (III.14) gives the critical scale.

Here and below  $\gamma$  denotes the hidden-to-visible spatial-mode ratio,  $\omega_d(u) = \gamma\omega_v(u)$ , fixed by Eq. (III.13). The HEE stress factor is

$$\mathcal{R}_{\text{HEE}}^{\text{II}} = 1 + \alpha_{\text{dm}}\gamma + \gamma^2. \quad (\text{II.63})$$

The mode composition is quantified by the hidden fraction  $f_d$ , which is displayed in Fig. 3.

We introduce a second SU(2) connection  $C_M^a\tau^a$  with field strength  $H_{MN}^a$ , coupled to the visible sector through a kinetic-mixing parameter  $\alpha_{\text{dm}}$ . The gauge-sector part of the action is

$$S_{\text{vis+dark}} = -\frac{1}{4} \int d^{d+2}x \sqrt{-g} e^{\lambda_{\text{YM}}\phi} (G_{MN}^a G^{aMN} + H_{MN}^a H^{aMN} + \alpha_{\text{dm}} G_{MN}^a H^{aMN}), \quad (\text{II.64})$$

The total action is obtained from  $S_0$  by replacing the visible  $G^2$  gauge-sector term in (II.1) with the bracket in (II.64). Equivalently, the gauge sector is  $S_{\text{vis}} + S_H + S_{\text{mix}}$ ; the visible  $G^2$  term is still present. We take the dark temporal ansatz  $C^a\tau^a = \eta(u)\tau^3 dt$ , so that  $H_{ut}^3 = \eta'(u)$  and all other components vanish.

*b. Temporal equations.* The original visible temporal equation  $\partial_u(\mathcal{P}_b b') - \mathcal{M}b\omega^2 = 0$  is deformed already before the spatial fluctuation is considered. Varying (II.64) with respect to  $b$  and  $\eta$  gives

$$\partial_u \left[ \mathcal{P}_b(u) \left( b' + \frac{\alpha_{\text{dm}}}{2} \eta' \right) \right] - \mathcal{M}(u)b\omega^2 = 0, \quad (\text{II.65})$$

$$\partial_u \left[ \mathcal{P}_b(u) \left( \eta' + \frac{\alpha_{\text{dm}}}{2} b' \right) \right] = 0. \quad (\text{II.66})$$

In the normal phase,  $\omega = 0$ , the second equation integrates to

$$\eta'(u) + \frac{\alpha_{\text{dm}}}{2} b'_0(u) = \frac{Q_X}{\mathcal{P}_b(u)}. \quad (\text{II.67})$$

The integration constant  $Q_X$ , together with the additive gauge constant, fixes the independent hidden chemical potential. For the minimal ensemble with no independent hidden source,  $Q_X = 0$ , and hence

$$\eta(u) = -\frac{\alpha_{\text{dm}}}{2} b_0(u) + c_X. \quad (\text{II.68})$$

In the boundary-source convention used for the two-parameter critical surface one writes  $c_X = \mu_X + \alpha_{\text{dm}}\sqrt{3}\mu/2$ , so that the independent source is  $\mu_X$ . In the horizon-regular solution convention used for the radial-solution checks, one instead sets  $c_X = 0$ , and the induced dark solution is simply  $\eta = -\alpha_{\text{dm}}b_0/2$ .

*c. Visible  $\omega$ -equation with mixing.* The coupled visible Yang–Mills equations obtained by varying  $B_M^a$  in (II.64) are

$$\nabla_M G^{aMN} + \frac{\alpha_{\text{dm}}}{2} \nabla_M H^{aMN} + \epsilon^{abc} B_M^b (G^{cMN} + \frac{\alpha_{\text{dm}}}{2} H^{cMN}) = 0, \quad (\text{II.69})$$

$$\nabla_M H^{aMN} + \frac{\alpha_{\text{dm}}}{2} \nabla_M G^{aMN} + \epsilon^{abc} C_M^b (H^{cMN} + \frac{\alpha_{\text{dm}}}{2} G^{cMN}) = 0. \quad (\text{II.70})$$

Substituting  $N = x_1$  and  $a = 1$  in (II.69), using  $H^{1Mx_1} = 0$  (since  $\eta$  has only  $a = 3$ ), the structure-constant terms yield

$$\epsilon^{132} B_t^3 G^{2tx_1} + \frac{\alpha_{\text{dm}}}{2} \epsilon^{132} C_t^3 G^{2tx_1} = -(b_0 + \frac{\alpha_{\text{dm}}}{2} \eta)(-b_0 \omega)(-g^{tt} g^{x_1 x_1}). \quad (\text{II.71})$$

The elimination is elementary but important, so we spell it out. In the  $N = x_1$ ,  $a = 1$  sector the two radial kinetic equations have the schematic matrix form

$$\begin{pmatrix} 1 & \alpha_{\text{dm}}/2 \\ \alpha_{\text{dm}}/2 & 1 \end{pmatrix} \begin{pmatrix} \nabla_M G^{1Mx_1} \\ \nabla_M H^{1Mx_1} \end{pmatrix} = \begin{pmatrix} \mathcal{J}_G \\ \mathcal{J}_H \end{pmatrix}, \quad \det = 1 - \frac{\alpha_{\text{dm}}^2}{4} \equiv \tilde{\alpha}. \quad (\text{II.72})$$

Multiplying the first row by one and subtracting  $\alpha_{\text{dm}}/2$  times the second row gives

$$\tilde{\alpha} \nabla_M G^{1Mx_1} = \mathcal{J}_G - \frac{\alpha_{\text{dm}}}{2} \mathcal{J}_H. \quad (\text{II.73})$$

Thus the visible kinetic operator is multiplied by  $\tilde{\alpha} = 1 - \alpha_{\text{dm}}^2/4$ , while the source terms generate the mixed radial contribution proportional to  $\eta b_0 \omega$ . The full reduced  $\omega$ -equation is

$$\partial_u(P \psi') + \frac{1}{\tilde{\alpha}} Q_{\text{vis}}(u; \mu) \psi - \frac{\alpha_{\text{dm}}^2}{4\tilde{\alpha}} Q_{\text{mix}}(u) \psi = 0, \quad (\text{II.74})$$

with

$$\tilde{\alpha} \equiv 1 - \frac{\alpha_{\text{dm}}^2}{4}, \quad Q_{\text{mix}}(u) \equiv \frac{u^{n_h-5} \eta(u) b_0(u)}{1 - u^{-n_h}}. \quad (\text{II.75})$$

The special minimal subfamily with no independent dark temporal source is still solvable, but not by setting the hidden spatial mode to zero. The off-diagonal kinetic term sources  $C_{x_1}^1$ , and the same hidden fluctuation also appears in the electric driving term. Thus  $\omega_d$  must be eliminated from the full coupled quadratic problem. The resulting constant-mode reduction is summarized in Eqs. (III.11)–(III.14) below.

*d. Two-component spatial eigenproblem.* If both visible and hidden spatial fluctuations are allowed,  $B_{x_1}^1 = \omega_v(u)$  and  $C_{x_1}^1 = \omega_d(u)$ , the critical mode becomes a two-component vector

$$\Psi(u) = \begin{pmatrix} \omega_v(u) \\ \omega_d(u) \end{pmatrix}, \quad (\text{II.76})$$

and the linearised problem takes the matrix Sturm–Liouville form

$$-\partial_u(\mathbb{P}(u) \partial_u \Psi) + \mathbb{V}(u) \Psi = \mu^2 \mathbb{W}(u) \Psi, \quad (\text{II.77})$$

with  $2 \times 2$  coefficient matrices  $\mathbb{P}$ ,  $\mathbb{V}$ ,  $\mathbb{W}$  whose off-diagonal entries are proportional to  $\alpha_{\text{dm}}$ . The composition of the lowest eigenmode is measured by the fractions

$$f_v = \frac{\int du \mathcal{W}_v \omega_v^2}{\int du (\mathcal{W}_v \omega_v^2 + \mathcal{W}_d \omega_d^2)}, \quad f_d = 1 - f_v, \quad (\text{II.78})$$

with the positive radial weight from the quadratic fluctuation norm. A lower eigenvalue with  $f_d \rightarrow 1$  is a dark-dominated instability, not a visible  $p$ -wave transition.

### 3. Case III-a: hidden dark scalar with a mass portal

Cases I and II add a second *gauge* sector. Case III instead adds a hidden *dark scalar*  $\Phi$ . The scalar is neutral under the visible  $SU(2)$ , so it has no adjoint covariant derivative and no visible flavor charge, but it is not part of the visible sector. On the boundary it is dual to a dark scalar operator  $\mathcal{O}_\Phi$ , and it communicates with the visible  $p$ -wave sector only through the  $\alpha_{\text{dm}}$ -controlled portal in Eq. (II.55). Its own action is

$$S_\Phi = -\frac{1}{2} \int d^{d+2}x \sqrt{-g} [g^{MN} \partial_M \Phi \partial_N \Phi + m_\Phi^2 e^{\lambda_\Phi \phi} \Phi^2], \quad \lambda_\Phi \phi \sqrt{2d(1+\theta)(\theta+z-1)} = -2\theta. \quad (\text{II.79})$$

The dilaton dressing is part of the definition of the sourced scalar deformation. It makes the covariant Klein–Gordon equation consistent with the HSV radial scaling used in the numerical boundary-value problem. The static equation is

$$\partial_u(\sqrt{-g} g^{uu} \Phi') - \sqrt{-g} m_\Phi^2 e^{\lambda_\Phi \phi} \Phi = 0. \quad (\text{II.80})$$

with *no*  $\epsilon^{abc} B^b \Phi^c$  adjoint coupling. The solution  $\Phi(u)$  carries the two falloffs of the dark scalar operator; in the numerical sourced problem we fix its UV coefficient and solve for the radial shape. Throughout the main susceptibility calculation the scalar solution is obtained from the sourced boundary-value problem described below. The scalar source fixes the external dark deformation, while the bulk equation determines the radial field that enters the portal.

The Case III-a portal is a mass-type coupling between the singlet and the visible gauge field,

$$S_{\text{portal}}^{(a)} = - \int d^{d+2}x \sqrt{-g} \alpha_{\text{dm}}^2 \lambda_{\Phi B} \Phi^2 B_M^a B^{aM}. \quad (\text{II.81})$$

For the  $p$ -wave ansatz  $B_M^a B^{aM} = g^{tt} b^2 + g^{x_1 x_1} \omega^2$ , so the portal contributes an *isotropic* positive mass. The visible radial equations become

$$\partial_u(\mathcal{P}_b b') - \mathcal{M} b \omega^2 = 0, \quad (\text{II.82})$$

$$\partial_u(\mathcal{P}_\omega \omega') + \mathcal{M} b^2 \omega - U_\Phi(u) \omega = 0, \quad U_\Phi(u) \equiv 2\alpha_{\text{dm}}^2 \lambda_{\Phi B} \sqrt{-g} g^{x_1 x_1} \Phi(u)^2. \quad (\text{II.83})$$

The added term is a positive mass for  $\omega$ , so the hidden scalar *raises* the critical chemical potential. Because  $\Phi$  is an isotropic singlet,  $U_\Phi$  is identical for every transverse orientation; the deformation is therefore null in the orientation-difference observable  $\mathcal{O}_{12}^{(2)}$  at leading order. Case III-a is thus a genuine *dark* deformation—a hidden dark operator  $\mathcal{O}_\Phi$  acting on the visible current sector—and not a scalar living inside the visible  $SU(2)$ .

In the present work the scalar solution is obtained from a sourced bulk scalar boundary-value problem rather than inserted by hand. Consequently any short-distance power law in the portal response should be read as the response to the chosen scalar dimension/solution. For a general normalizable solution  $\Phi \sim u^{-\Delta_\Phi}$ , the short-strip power is expected to depend on  $\Delta_\Phi$ . We therefore do not interpret any single model, including  $\Delta_\Phi = 2$  in the exponent scan or  $\Delta_\Phi = 1.10$  in the displayed Case-III-b response scan, as a universal property of all dark scalars.

4. *Case III-b: hidden dark scalar with a gauge-kinetic portal*

Case III-b couples the same hidden singlet  $\Phi$  to the visible Yang–Mills kinetic term through a scalar-dependent prefactor,

$$S_{\text{portal}}^{(b)} = -\frac{1}{4} \int d^{d+2}x \sqrt{-g} Z_{\text{dm}}(\Phi) e^{\lambda_{\text{YM}}\phi} G_{MN}^a G^{aMN}, \quad Z_{\text{dm}}(\Phi) = 1 + \lambda_Z \Phi^2 + O(\lambda_Z^2). \quad (\text{II.84})$$

Since  $\Phi$  is a singlet,  $Z_{\text{dm}}(\Phi)$  is color-blind: it multiplies every color component of the field strength equally, so there is no adjoint  $Z_{\parallel}/Z_{\perp}$  splitting. The portal reweights the radial kinetic and electric terms by the common  $u$ -dependent factor  $Z_{\text{dm}}(\Phi(u))$ ,

$$\partial_u(Z_{\text{dm}}(\Phi) \mathcal{P}_b b') - Z_{\text{dm}}(\Phi) \mathcal{M} b \omega^2 = 0, \quad (\text{II.85})$$

$$\partial_u(Z_{\text{dm}}(\Phi) \mathcal{P}_\omega \omega') + Z_{\text{dm}}(\Phi) \mathcal{M} b^2 \omega = 0. \quad (\text{II.86})$$

At the normal phase,  $\omega = 0$ , the temporal equation must first be solved with the same kinetic factor. Writing the boundary value as  $b_\infty = \sqrt{3} \mu$ , the horizon-regular solution is

$$b_0^{(Z)}(u) = b_\infty \frac{\int_1^u \frac{dv}{Z_{\text{dm}}(\Phi(v)) \mathcal{P}_b(v)}}{\int_1^\infty \frac{dv}{Z_{\text{dm}}(\Phi(v)) \mathcal{P}_b(v)}} \equiv b_\infty \widehat{b}_Z(u). \quad (\text{II.87})$$

Thus the portal changes the shape of  $b_0$ ; keeping the visible power law while changing only the spatial equation would be inconsistent at the same order in the portal strength.

Linearising the spatial equation as  $\omega = \epsilon \psi + O(\epsilon^3)$  gives the self-adjoint problem

$$\partial_u[Z_{\text{dm}}(\Phi(u)) \mathcal{P}_\omega(u) \psi'(u)] + b_\infty^2 Z_{\text{dm}}(\Phi(u)) \mathcal{M}(u) \widehat{b}_Z(u)^2 \psi(u) = 0. \quad (\text{II.88})$$

The corresponding critical boundary amplitude is

$$b_{\infty,c}^2 = \min_{\psi_{\text{src}}=0} \frac{\int_1^\infty du Z_{\text{dm}}(\Phi) \mathcal{P}_\omega (\psi')^2}{\int_1^\infty du Z_{\text{dm}}(\Phi) \mathcal{M} \widehat{b}_Z^2 \psi^2}, \quad \mu_c = \frac{b_{\infty,c}}{\sqrt{3}}. \quad (\text{II.89})$$

Both the explicit factor  $Z_{\text{dm}}$  and the induced change of  $\widehat{b}_Z$  enter the same eigenvalue problem. Consequently, the sign of the critical-point shift is not fixed by a simple numerator-versus-denominator argument. For the dynamical sourced scalar-solution family used below, positive  $\lambda_Z$  raises  $\mu_c$  at the three analytic reference backgrounds, while the wider  $(\theta, z)$  scan contains regions in which the shift changes sign. The kinetic portal is non-null in  $\mathcal{O}_{12}^{(2)}$  because the same self-consistent  $b_0^{(Z)}$  and  $\psi_Z$  solutions change the traceless Yang–Mills source. The size of this effect is measured by the derivative susceptibility in Sec. IV.C.

*a. Radial equations entering the RT response.* For transparency we collect the one-dimensional radial equations that underlie the RT response. These are not phenomenological fitting equations. They are obtained by inserting the component field strengths in Eq. (II.21) and their dark-sector analogues into the bulk action, reducing to a radial functional, and varying the radial fields. The analytic reductions and numerical boundary-value problems start from the following radial systems.

The visible reference system is

$$\partial_u(\mathcal{P}_b b') - \mathcal{M}b\omega^2 = 0, \quad \partial_u(\mathcal{P}_\omega \omega') + \mathcal{M}b^2\omega = 0. \quad (\text{II.90})$$

The normal electric solution obeys  $\partial_u(\mathcal{P}_b b'_0) = 0$ , hence Eq. (II.31); the linear zero-mode threshold mode obeys Eq. (II.32).

Case I adds the temporal hidden Abelian field  $x(u)$ . The component equations are

$$\partial_u(\mathcal{P}_b b' + \chi \mathcal{P}_m x') - \mathcal{M}b\omega^2 = 0, \quad (\text{II.91})$$

$$\partial_u(\mathcal{P}_X x' + \chi \mathcal{P}_m b') = 0, \quad (\text{II.92})$$

$$\partial_u(\mathcal{P}_\omega \omega') + \mathcal{M}b^2\omega = 0. \quad (\text{II.93})$$

The hidden electric equation has the first integral

$$\mathcal{P}_X x'(u) + \chi \mathcal{P}_m b'(u) = Q_X, \quad x'(u) = \frac{Q_X - \chi \mathcal{P}_m b'(u)}{\mathcal{P}_X}. \quad (\text{II.94})$$

Thus Case I modifies the normal electric solution  $b_X(u)$  through the coupled temporal sector. It does not introduce a new spatial vector order or a direct anisotropic mass for  $\omega$ . After  $b_X$  is fixed, the source-free critical-mode problem equation is  $\partial_u(\mathcal{P}_\omega \psi'_X) + \mathcal{M}b_X^2 \psi_X = 0$ . If the same visible temporal component is used for a leading orientation-difference comparison, the RT anisotropic source is the visible one and the case is null in  $O_{12}^{(2)}$ .

Case II uses the visible and hidden temporal components  $b(u), \eta(u)$  and, at the critical threshold, the two spatial solutions  $\omega_v(u), \omega_d(u)$ . To quadratic order in the spatial modes the component radial equations are

$$\partial_u \left[ \mathcal{P}_b \left( b' + \frac{\alpha_{\text{dm}}}{2} \eta' \right) \right] - \mathcal{M} \left( b\omega_v^2 + \frac{\alpha_{\text{dm}}}{2} \eta \omega_v \omega_d \right) = 0, \quad (\text{II.95})$$

$$\partial_u \left[ \mathcal{P}_b \left( \eta' + \frac{\alpha_{\text{dm}}}{2} b' \right) \right] - \mathcal{M} \left( \eta \omega_d^2 + \frac{\alpha_{\text{dm}}}{2} b \omega_v \omega_d \right) = 0, \quad (\text{II.96})$$

$$\partial_u \left[ \mathcal{P}_\omega \left( \omega'_v + \frac{\alpha_{\text{dm}}}{2} \omega'_d \right) \right] + \mathcal{M} \left( b^2 \omega_v + \frac{\alpha_{\text{dm}}}{2} b \eta \omega_d \right) = 0, \quad (\text{II.97})$$

$$\partial_u \left[ \mathcal{P}_\omega \left( \omega'_d + \frac{\alpha_{\text{dm}}}{2} \omega'_v \right) \right] + \mathcal{M} \left( \eta^2 \omega_d + \frac{\alpha_{\text{dm}}}{2} b \eta \omega_v \right) = 0. \quad (\text{II.98})$$

The normal-phase critical-mode limit drops the terms quadratic in  $\omega_{v,d}$  from Eqs. (II.95) and (II.96). In the minimal no-independent-hidden-source ensemble, the remaining temporal equations give  $\eta = -\alpha_{\text{dm}} b_0/2$  up to a gauge constant. Substituting the constant-ratio ansatz

$\omega_d = \gamma(\alpha_{\text{dm}})\omega_v$  in Eqs. (II.97) and (II.98) reduces the matrix boundary-value problem to Eq. (III.13) and the critical law in Eq. (III.14). The RT source is then multiplied by  $1 + \alpha_{\text{dm}}\gamma + \gamma^2$ .

Case III-a first solves the sourced dark-scalar boundary-value problem

$$\partial_u(\sqrt{-g}g^{uu}\Phi') - \sqrt{-g}m_{\Phi}^2 e^{\lambda_{\Phi\phi}\phi}\Phi = 0. \quad (\text{II.99})$$

The mass-portal critical-mode equation used in the null-orientation comparison is

$$\partial_u(\mathcal{P}_b b') = 0, \quad \partial_u(\mathcal{P}_\omega \psi') + \mathcal{M}b^2\psi - U_{\Phi}(u)\psi = 0, \quad (\text{II.100})$$

with

$$U_{\Phi}(u) = 2\alpha_{\text{dm}}^2 \lambda_{\Phi B} \sqrt{-g}g^{x_1 x_1} \Phi(u)^2. \quad (\text{II.101})$$

This portal is isotropic in the boundary spatial directions because  $\Phi$  is a singlet. It can shift the scalar cost of the vector critical threshold, but it does not produce a leading traceless orientation source by itself, so it is null in  $O_{12}^{(2)}$  at the order used for the figures.

Case III-b uses the same scalar BVP but inserts the gauge-kinetic factor before solving either Yang–Mills solution:

$$\partial_u[Z_{\text{dm}}(\Phi)\mathcal{P}_b b'] - Z_{\text{dm}}(\Phi)\mathcal{M}b\omega^2 = 0, \quad (\text{II.102})$$

$$\partial_u[Z_{\text{dm}}(\Phi)\mathcal{P}_\omega \omega'] + Z_{\text{dm}}(\Phi)\mathcal{M}b^2\omega = 0, \quad (\text{II.103})$$

$$\partial_u(\sqrt{-g}g^{uu}\Phi') - \sqrt{-g}m_{\Phi}^2 e^{\lambda_{\Phi\phi}\phi}\Phi = 0. \quad (\text{II.104})$$

On the normal phase, Eq. (II.102) integrates analytically to the solution in Eq. (II.87); the source-free critical-mode problem then solves Eq. (II.88). The radial stress inserted into the RT variation is

$$S_{\text{aniso}}^{\text{IIIb}}(u) = Z_{\text{dm}}(\Phi(u)) \left[ u^{d\theta+d+3z-3} N_0(u) \psi'_Z(u)^2 - u^{d\theta+z+d-5} \frac{b_Z(u)^2 \psi_Z(u)^2}{N_0(u)} \right], \quad (\text{II.105})$$

which is the same component expression used later in Eq. (IV.59). This is the analytic-to-numerical boundary of the calculation: the radial equations, first integrals, and the component RT source are fixed analytically. The shipped dense tables then evaluate the scalar BVP and the leading short-width response described below; they do not rely on a fitted radial field.

### III. VISIBLE HSV SCALING AND DARK-SECTOR RESPONSE

The purpose of this section is not to single out one hidden sector as the whole content of the paper. The coupled hidden-SU(2) eigenvalue law is one analytically solvable model. The broader question is how the visible  $p$ -wave critical point, which already depends nontrivially on the HSV exponents, is modified when extra hidden gauge or scalar sectors deform the radial operator. We therefore proceed in three steps. First we recall the visible, dark-free scaling problem and explain how HSV geometry changes the critical scale relative to the isotropic AdS case. Second we write a general operator-level formula for how a dark deformation shifts the critical eigenvalue. Third we identify the minimal hidden-SU(2) case as the special subcase in which that general shift collapses to a closed coupled-mode law.

### III.A. Visible critical point before dark-sector deformation

Without any dark sector the source-free vector mode obeys the Sturm–Liouville problem (II.32). It is useful to rewrite it in the standard self-adjoint form

$$-\partial_u(P(u)\psi'(u)) = \mu^2 W_0(u)\psi(u), \quad W_0(u) \equiv \frac{Q(u; \mu)}{\mu^2}. \quad (\text{III.1})$$

The corresponding Rayleigh quotient is

$$\mu_{c,\text{vis}}^2(d, z, \theta) = \min_{\psi_{\text{src}}=0} \frac{\int_1^\infty du P(u)(\psi')^2}{\int_1^\infty du W_0(u)\psi^2}. \quad (\text{III.2})$$

This equation already contains the first scaling effect of the paper. In an isotropic AdS  $p$ -wave model one has  $z = 1$  and  $\theta = 0$ , so the powers entering  $P$  and  $W_0$  are fixed by the boundary dimension alone. In an HSV geometry these weights instead contain

$$n_h = d\theta + z + d, \quad n_p = d\theta + d + 3z - 3, \quad (\text{III.3})$$

and therefore both the kinetic weight and the electric driving weight are reshaped by  $(z, \theta)$ . Thus even the visible theory has a nontrivial HSV critical point surface,

$$\mu_{c,\text{vis}} = \mu_{c,\text{vis}}(D, z, \theta), \quad (\text{III.4})$$

rather than a single AdS critical number.

The physical transition scale follows from the horizon scaling. If  $\tilde{\mu}$  denotes the physical boundary chemical potential and  $\mu$  the dimensionless eigenvalue used in the radial problem, then

$$\tilde{\mu} \propto r_h^{n_h-2} \mu, \quad T = \frac{n_h}{4\pi} r_h^z. \quad (\text{III.5})$$

At fixed physical chemical potential this gives, up to the same normalization used in the radial ansatz,

$$T_{c,\text{vis}}(D, z, \theta; \tilde{\mu}) = \frac{n_h}{4\pi} \left( \frac{\tilde{\mu}}{\mu_{c,\text{vis}}(D, z, \theta)} \right)^{z/(n_h-2)}. \quad (\text{III.6})$$

Equation (III.6) is the baseline scaling law before any hidden deformation is added. The role of the dark sector is to replace  $\mu_{c,\text{vis}}$  by a deformed eigenvalue and, if the deformation changes the operator shape, to modify the radial field that sources the HEE and probe free-energy checks.

### III.B. General dark-sector deformation of the critical operator

A general dark deformation changes the self-adjoint problem in one of three ways:

$$P(u) \longrightarrow P(u) + \delta P(u), \quad W_0(u) \longrightarrow W_0(u) + \delta W(u), \quad U(u) \neq 0. \quad (\text{III.7})$$

Here  $\delta P$  changes the radial kinetic weight of the vector zero mode,  $\delta W$  changes the electric driving weight, and  $U$  denotes an additional mass or cost term generated by an isotropic scalar background or by a scalar portal contribution. The deformed eigenvalue can be written as

$$\mu_c^2 = \min_{\psi_{\text{src}}=0} \frac{\int_1^\infty du [(P + \delta P)(\psi')^2 + U\psi^2]}{\int_1^\infty du (W_0 + \delta W)\psi^2}. \quad (\text{III.8})$$

For a small deformation, evaluating the first variation on the undeformed normalizable zero mode  $\psi_0$  gives

$$\delta\mu_c^2 = \frac{\int_1^\infty du [\delta P(\psi_0')^2 + U\psi_0^2 - \mu_{c,\text{vis}}^2 \delta W \psi_0^2]}{\int_1^\infty du W_0 \psi_0^2} + O(\delta^2). \quad (\text{III.9})$$

This formula is the useful organizing principle. A deformation that increases  $\delta P$  or adds a positive  $U$  tends to raise the critical point. A deformation that increases the electric driving weight  $\delta W$  tends to lower it. If the deformation is proportional to  $W_0$  everywhere, the shift is a global rescaling. If it is  $u$ -dependent, as in the gauge-kinetic portal, the response is radially dependent and cannot be reduced to one universal number.

The four cases of Sec. II occupy different positions in this operator language:

- **Case I** changes the temporal/electric sector through a hidden  $U(1)$  solution but does not add a new anisotropic vector mass term. At leading order it is therefore largely a temporal-sector deformation and is null in the orientation-difference HEE coefficient.
- **Case II** with  $\mu_X = 0$  is the exceptional case in which the change is exactly proportional to  $W_0$ ; it becomes a global rescaling of  $\mu^2$ .
- **Case III-a** adds a positive scalar cost  $U_\Phi$  to the vector operator. It can move the critical point, but because the scalar background is isotropic it cancels in  $S_\perp - S_\parallel$  at leading order.
- **Case III-b** modifies  $P$  and  $W_0$  through the single colour-blind radial factor  $Z_{\text{dm}}(\Phi(u))$  of the hidden dark-scalar kinetic portal. Its effect is therefore non-universal and must be computed from the full radial source.

Thus the hidden-SU(2) law below should be read as one solvable corner of a broader response classification, not as the organizing principle of the entire paper.

### III.C. Minimal hidden SU(2) mixing model

For the minimal hidden-SU(2) kinetic-mixing ensemble with no independent hidden chemical potential, the critical fluctuation is a genuine two-vector mode. The hidden spatial fluctuation

must be included in the full quadratic problem and then diagonalized together with the visible fluctuation. Let  $a \equiv \alpha_{\text{dm}}$  and denote the visible and hidden spatial zero modes by  $\omega_v$  and  $\omega_d$ . After the induced hidden temporal background is inserted, the coupled zero-mode equations have the form

$$\partial_u \left[ P \left( \omega'_v + \frac{a}{2} \omega'_d \right) \right] + M b_0^2 \left( \omega_v - \frac{a^2}{4} \omega_d \right) = 0, \quad (\text{III.10})$$

$$\partial_u \left[ P \left( \omega'_d + \frac{a}{2} \omega'_v \right) \right] + \frac{a^2}{4} M b_0^2 (\omega_d - \omega_v) = 0. \quad (\text{III.11})$$

The important simplification is that the radial weights are common to the two channels. Therefore a constant mixing ansatz

$$\omega_d(u) = \gamma(a) \omega_v(u) \quad (\text{III.12})$$

closes the eigenvalue problem. The physical root is the regular root of

$$\frac{a^2}{4} \left( 1 + \frac{a}{2} \right) \gamma^2 - \left( 1 - \frac{a^2}{4} \right) \gamma - \left( \frac{a}{2} + \frac{a^2}{4} \right) = 0. \quad (\text{III.13})$$

The critical chemical potential is then

$$\frac{\mu_c(a)}{\mu_c(0)} = \left( \frac{1 + \frac{a}{2} \gamma(a)}{1 - \frac{a^2}{4} \gamma(a)} \right)^{1/2}. \quad (\text{III.14})$$

For the representative values used in the figures one finds

$a$	0.4	0.8	1.0	1.2	(III.15)
$\mu_c(a)/\mu_c(0)$	0.9702	0.8390	0.7320	0.6126	

at the analytic reference background. On the boundary side, this should not be oversimplified as a single scalar deformation  $S_{\text{CFT}} + \alpha_{\text{dm}} \int \mathcal{O}_{\text{hidden}}$ . The more faithful interpretation is a current-sector portal. Schematically, the leading local term in an effective boundary description may be written as

$$S_{\text{eff}} = S_{\text{HSV}}^{\text{vis}}[J_{\text{vis}}] + S_{\text{HSV}}^{\text{hid}}[J_X] + \frac{\alpha_{\text{dm}}}{2} \int d^{d+1}x \sqrt{-g_{(0)}} g_{(0)}^{\mu\nu} \delta_{ab} J_{\text{vis}\mu}^a J_{X\nu}^b + \dots \quad (\text{III.16})$$

Here  $g_{(0)\mu\nu}$  is the boundary metric representative,  $d = D - 2$  is the number of boundary spatial directions,  $\mu, \nu$  run over boundary time and space, and  $a, b = 1, 2, 3$  are adjoint flavor indices for the hidden-SU(2) version of Case II. The notation  $S_{\text{HSV}}^{\text{vis/hid}}$  denotes the effective generating functional of the visible or hidden current sector in the HSV scaling regime, not a microscopic UV Lagrangian. For the Abelian hidden-current case one simply drops the adjoint index on  $J_X$ . The ellipsis represents higher-derivative terms, multi-current operators and local counterterms that do not enter the leading two-current mixing considered here; the factor  $\alpha_{\text{dm}}/2$  matches the normalization of the bulk kinetic-mixing term. In the bulk variational problem the canonical momenta dual to  $J_{\text{vis}}$  and  $J_X$  are mixed. If the hidden source is set to zero, integrating out

or eliminating the hidden channel induces an effective deformation of the visible current two-point function. In a UV-complete boundary theory such a portal may run under RG. In our bottom-up HSV description,  $\alpha_{\text{dm}}$  is treated as a fixed coupling of the finite-density scaling regime, while the holographic radial evolution computes the resulting scale dependence of the response. The special feature of Case II is that this flow still collapses to a closed two-channel eigenvalue problem. This is precisely why it remains a useful analytic model: the visible and hidden channels share a single radial eigenfunction.

Combining this with the baseline horizon scaling (III.6) gives

$$\frac{T_c(a)}{T_c(0)} = \left[ \frac{\mu_c(a)}{\mu_c(0)} \right]^{-\frac{z}{n_h-2}}, \quad \frac{\mu_c(a)}{\mu_c(0)} \text{ given by Eq. (III.14)}. \quad (\text{III.17})$$

This is why the hidden-SU(2) sector is useful: it supplies an analytic reference curve against which the numerical figures can be read. It is not, by itself, a general theorem for all dark deformations. The proof works because the coupled visible–hidden channel has a constant mixing ratio and does not introduce a new radial function.

*Loss of the closed algebraic law.* The closed algebraic law is lost whenever the dark sector introduces a new radial shape or a second boundary scale. The cleanest example is Case II with an independent hidden chemical potential. On the  $D = 4$  analytic reference sector  $(d, z, \theta) = (2, 1, 1/2)$  the reduced critical-point equation becomes

$$\frac{\mu_c^2 - (\alpha_{\text{dm}}^2/4)\mu_c\nu}{\tilde{\alpha}} = \frac{16}{3}, \quad (\text{III.18})$$

where  $\nu \equiv \mu_X$  is the independent hidden chemical potential. The solution is

$$\mu_c(\alpha_{\text{dm}}, \nu) = \frac{1}{2} \left[ \frac{\alpha_{\text{dm}}^2}{4}\nu + \sqrt{\frac{\alpha_{\text{dm}}^4}{16}\nu^2 + \frac{64}{3}\tilde{\alpha}} \right]. \quad (\text{III.19})$$

At  $\nu = 0$  this must be compared with the coupled-mode law in Eq. (III.14); at  $\nu \neq 0$  the additional term cannot be absorbed into a single visible-channel electric weight. The scalar mass portal and the scalar gauge-kinetic portal break the exact law for a different reason: they change the radial operator itself. In the language of Eq. (III.9), Case III-a contributes a positive  $U_\Phi$ , while Case III-b produces  $u$ -dependent changes in  $\delta P$ ,  $\delta W$ , and  $U_\Phi/Z_1$ .

This is the conceptual distinction used in the final figure set. Case II is shown with explicit  $\alpha_{\text{dm}}$  coupled-mode factors because its effect is analytic. The other cases are shown through their dark-minus-visible radial sources, critical values and HEE shifts because their response is not captured by a one-parameter scaling law.

#### IV. RT SURFACES, HEE RESPONSE, AND THE CONDENSATE

The previous sections define the visible and dark-deformed radial equations and the critical scale  $\mu_c$ . This section explains the ordered-phase observables used in the figures. Its purpose

is not to build a separate full phase diagram, but to make clear why HEE is a useful geometric probe, how the boundary regions are chosen, how the dark-sector radial source enters the RT variation, how the entanglement first-law check is normalised, and how the condensate  $\langle O \rangle$  is extracted from the nonlinear solution family.

#### IV.A. RT observables: interval, strip, slab, and orientation anisotropy

The visible ordered phase is anisotropic because the bulk field contains  $B_{x_1}^1 = \omega(u)$ . A critical chemical potential detects when this vector mode becomes normalizable, but it does not by itself measure how strongly the ordered state distinguishes the direction parallel to the condensate from transverse directions. HEE is sensitive to that distinction because the boundary entangling region can be oriented with respect to the vector order.

In  $D = 3$  the boundary has one spatial direction, and the entangling region is a line segment of length  $\ell$ . We write

$$\Delta S_{\text{int}} = \delta^2 \epsilon^2 \Delta S_{\text{int}}^{(2)} + O(\epsilon^4). \quad (\text{IV.1})$$

For  $D = 4, 5$  the region is a strip or slab: one direction has finite width  $W$ , while the remaining spectator directions are regulated by a transverse volume. If those spectator directions are compactified, the same construction may be viewed as a cylinder-like RT surface. The physical datum is the orientation of the finite-width direction. We compare a strip parallel to the condensate with a strip transverse to it and define

$$\mathcal{O}_{12}^{\text{EE}} = S_{\perp} - S_{\parallel} = \delta^2 \epsilon^2 \mathcal{O}_{12}^{(2)} + O(\epsilon^4). \quad (\text{IV.2})$$

This is the signed observable used in the corrected  $D = 4, 5$  figures. It is not a ratio.

Before any dark deformation is inserted, the RT surface is computed in the isotropic HSV seed geometry. We derive the strip-width formula from the area functional, rather than using it as an input. Choose the finite-width direction to be  $x \equiv x_1$ , take the spectator directions  $x_2, \dots, x_d$  to have regulated volume  $V_{\perp}$ , and parametrize one half of the surface by  $x = x(u)$  at fixed time. From Eq. (II.8), with  $N_0(u) = 1 - u^{-n_h}$ , the induced metric on this surface is

$$\gamma_{uu}^{(0)} = r_h^{2\theta} u^{2\theta} \left( \frac{1}{u^2 N_0(u)} + u^2 x'(u)^2 \right), \quad \gamma_{ab}^{(0)} = r_h^{2\theta} u^{2\theta+2} \delta_{ab}, \quad a, b = 2, \dots, d. \quad (\text{IV.3})$$

After dividing by the spectator volume and the overall power of  $r_h$ , the area functional is

$$\frac{\mathcal{A}_0}{V_{\perp}} = 2 \int_{u_*}^{\infty} du \mathcal{L}_0, \quad \mathcal{L}_0 = \frac{u^{d(1+\theta)-2}}{\sqrt{N_0(u)}} \sqrt{1 + u^4 N_0(u) x'(u)^2}. \quad (\text{IV.4})$$

The factor of two accounts for the two symmetric halves of the surface. Since  $x$  does not appear explicitly in  $\mathcal{L}_0$ , the conjugate momentum is conserved:

$$\Pi_x \equiv \frac{\partial \mathcal{L}_0}{\partial x'} = \frac{u^{d(1+\theta)+2} \sqrt{N_0(u)} x'}{\sqrt{1 + u^4 N_0(u) x'^2}}. \quad (\text{IV.5})$$

At the turning point  $u = u_*$ , the surface is vertical in the  $(u, x)$  plane, so  $x'(u) \rightarrow \infty$ . Equation (IV.5) then fixes the conserved momentum to be

$$\Pi_x = u_*^{d(1+\theta)}. \quad (\text{IV.6})$$

Solving Eq. (IV.5) for  $x'(u)$  gives

$$x'(u) = \frac{u_*^{d(1+\theta)}}{u^{d(1+\theta)+1} \sqrt{N_0(u)} \sqrt{1 - (u_*/u)^{2d(1+\theta)}}}. \quad (\text{IV.7})$$

The boundary separation is therefore

$$W(u_*) = 2 \int_{u_*}^{\infty} du x'(u) = 2 \int_{u_*}^{\infty} du \frac{u_*^{d(1+\theta)}}{u^{d(1+\theta)+1} N_0(u)^{1/2} \sqrt{1 - (u_*/u)^{2d(1+\theta)}}}. \quad (\text{IV.8})$$

The finite part of the undeformed strip entropy is written below in Eq. (IV.74). For the dark-sector comparison we use the RT first variation rather than subtracting two large nonlinear areas after the fact. The logic has three steps. First, the order- $\epsilon^2$  Yang–Mills stress sources the order- $\epsilon^2$  metric response,

$$g_{MN} = g_{MN}^{(0)} + \delta^2 \epsilon^2 g_{MN}^{(2)} + O(\epsilon^4), \quad \phi = \phi_0 + \delta^2 \epsilon^2 \phi_2 + O(\epsilon^4), \quad (\text{IV.9})$$

through the linearized Einstein equation

$$\mathcal{E}_{MN}^{\text{lin}}[g^{(2)}, \phi_2] = T_{MN}^{(2)}. \quad (\text{IV.10})$$

Second, only the traceless spatial part of this equation can affect the difference between the two strip orientations. The spatial metric perturbation can always be decomposed into a part common to all boundary spatial directions and a traceless part. The common part gives the same first-order area shift for the parallel and transverse strips and cancels in  $S_{\perp} - S_{\parallel}$ . The traceless part is controlled by the Einstein-equation difference

$$\mathcal{E}^{x_1}_{x_1} - \mathcal{E}^{x_2}_{x_2} = T^{x_1}_{x_1} - T^{x_2}_{x_2}. \quad (\text{IV.11})$$

In our radial gauge this traceless metric perturbation is denoted by  $A_2(u)$ , and Eq. (IV.11) reduces to

$$[u^{d\theta+z+d+1} N_0(u) A_2'(u)]' = k_D S_{\text{aniso}}(u), \quad k_4 = -\frac{1}{4}, \quad k_5 = \frac{1}{3}. \quad (\text{IV.12})$$

Here  $S_{\text{aniso}}$  is the radial measure times  $T^{x_1}_{x_1} - T^{x_2}_{x_2}$ . If the extra dark-sector stress has zero value in this traceless combination, then the corresponding change of  $A_2$  obeys the homogeneous version of Eq. (IV.12). With the same regularity condition at the horizon and the same no-source condition at the boundary, the homogeneous solution is zero. Hence that dark sector changes neither the traceless metric perturbation nor the strip orientation difference at this order.

Third, the RT surface measures this metric perturbation. For a fixed undeformed RT surface  $\Sigma_0$ , with intrinsic coordinates  $\sigma^a$ , we denote its bulk embedding by  $Y^M(\sigma)$ . This embedding coordinate is unrelated to the dark-case label  $X$ . The first variation of the RT area is

$$\delta S_{\text{RT}} = \frac{1}{8G_D} \int_{\Sigma_0} d^{D-2} \sigma \sqrt{\gamma^{(0)}} \gamma_{(0)}^{ab} g_{MN}^{(2)} \partial_a Y^M \partial_b Y^N. \quad (\text{IV.13})$$

Thus the complete chain is

$$T^{x_1}_{x_1} - T^{x_2}_{x_2} \longrightarrow A_2(u) \longrightarrow S_{\perp}^{(2)}(W) - S_{\parallel}^{(2)}(W). \quad (\text{IV.14})$$

This is the reason we compute the traceless stress source before doing the RT integral. For orientation  $n = \parallel, \perp$  and dark case  $X$ , we define

$$S_n^{(2),X}(W) \equiv \delta S_{\text{RT}}[\Sigma_0 = \Sigma_n^{(0)}(W), g^{(2)} = g^{(2),X}]. \quad (\text{IV.15})$$

The displayed observables are then

$$\Delta S_{\text{int}}^{(2),X} = S_{\text{int}}^{(2),X} \quad (D=3), \quad \mathcal{O}_{12}^{(2),X}(W) = S_{\perp}^{(2),X}(W) - S_{\parallel}^{(2),X}(W) \quad (D=4,5). \quad (\text{IV.16})$$

For the scalar-portal scan we use the perturbative short-width reduction described below, because direct subtraction of nearly equal oriented RT areas is ill-conditioned in that channel.

We now derive the local source  $S_{\text{aniso}}$  explicitly for the visible p-wave field. The visible ansatz has

$$G_{ut}^3 = b'_0(u), \quad G_{ux_1}^1 = w'_1(u), \quad G_{tx_1}^2 = -b_0(u)w_1(u). \quad (\text{IV.17})$$

The first component is the normal electric background and has no boundary spatial index. It is therefore isotropic in the boundary spatial directions and drops out of the difference between the direction of the condensate and a transverse direction. The only field strengths that can distinguish  $x_1$  from  $x_2$  are

$$G_{x_1u}^1 = -w'_1(u), \quad G_{x_1t}^2 = b_0(u)w_1(u), \quad G_{x_2P}^a = 0 \quad \text{at order } w_1. \quad (\text{IV.18})$$

The Yang–Mills stress tensor has the standard form

$$T^i_j|_{\text{YM}} = e^{\lambda_{\text{YM}}\phi} \left( g^{ik} G_{kP}^a G_j^{aP} - \frac{1}{4} \delta^i_j G_{MN}^a G^{aMN} \right), \quad i, j = 1, \dots, d. \quad (\text{IV.19})$$

Keeping only the order- $w_1^2$  terms, the trace piece in Eq. (IV.19) is the same for  $T^{x_1}_{x_1}$  and  $T^{x_2}_{x_2}$ , so it cancels in the traceless combination. To see this term by term, write the two diagonal components as

$$T^{x_1}_{x_1}|_{w_1^2} = e^{\lambda_{\text{YM}}\phi} g^{x_1x_1} [g^{uu} (G_{x_1u}^1)^2 + g^{tt} (G_{x_1t}^2)^2] - \frac{1}{4} e^{\lambda_{\text{YM}}\phi} G^2|_{w_1^2}, \quad (\text{IV.20})$$

$$T^{x_2}_{x_2}|_{w_1^2} = -\frac{1}{4} e^{\lambda_{\text{YM}}\phi} G^2|_{w_1^2}, \quad (\text{IV.21})$$

where  $G^2 \equiv G_{MN}^a G^{aMN}$ . Subtracting gives

$$T^{x_1}_{x_1} - T^{x_2}_{x_2} = e^{\lambda_{\text{YM}}\phi} g^{x_1 x_1} [g^{uu} w_1'^2 + g^{tt} b_0^2 w_1^2]. \quad (\text{IV.22})$$

Because  $g^{tt} < 0$ , the second term is the electric contribution with the opposite sign. Multiplying by the common radial measure appearing in the Einstein equation and using the definitions of the radial weights,

$$\mathcal{P}_\omega = \sqrt{-g} e^{\lambda_{\text{YM}}\phi} g^{uu} g^{x_1 x_1}, \quad \mathcal{M} = \sqrt{-g} e^{\lambda_{\text{YM}}\phi} (-g^{tt}) g^{x_1 x_1}, \quad (\text{IV.23})$$

we obtain the source used in Eq. (IV.12):

$$S_{\text{aniso}}(u) = \mathcal{P}_\omega w_1'(u)^2 - \mathcal{M} b_0(u)^2 w_1(u)^2 = u^{d\theta+d+3z-3} N_0(u) w_1'(u)^2 - u^{d\theta+z+d-5} \frac{b_0(u)^2 w_1(u)^2}{N_0(u)}. \quad (\text{IV.24})$$

Thus the first term is the radial magnetic contribution of  $G_{ux_1}^1$ , and the second term is the non-Abelian electric contribution of  $G_{tx_1}^2$ . This is the local traceless source that must be identified for each dark case before any RT integral is evaluated.

For clarity we spell out how the dark-sector radial equations enter the RT source. The orientation difference is not sourced by every change of the matter sector. It is sourced only by the order- $\epsilon^2$  part of the stress tensor that distinguishes the condensate direction  $x_1$  from a transverse direction  $x_2$ . Thus, before doing the RT integral, we identify the local traceless spatial source that appears in Eq. (IV.12). Let  $\psi_X$  denote the source-free spatial zero mode in dark case  $X$ , with the same UV normalization convention used for the plotted ratios. The visible reference obeys

$$\partial_u(\mathcal{P}_b b_0') = 0, \quad (\text{IV.25})$$

$$\partial_u(\mathcal{P}_\omega \psi_{\text{vis}}') + \mathcal{M} b_0^2 \psi_{\text{vis}} = 0, \quad (\text{IV.26})$$

$$S_{\text{aniso}}^{\text{vis}}(u) = \mathcal{P}_\omega \psi_{\text{vis}}'^2 - \mathcal{M} b_0^2 \psi_{\text{vis}}^2. \quad (\text{IV.27})$$

The first term in  $S_{\text{aniso}}^{\text{vis}}$  comes from the radial magnetic field strength  $G_{ux_1}^1$ . The second comes from the non-Abelian electric field strength  $G_{tx_1}^2$ . These are the visible components that carry the special boundary index  $x_1$ , and therefore they are the components that can contribute to  $T^{x_1}_{x_1} - T^{x_2}_{x_2}$ .

Case I adds a hidden Abelian temporal component  $x(u)$ , but no hidden spatial vector order. The radial equations are

$$\partial_u(\mathcal{P}_b b_X' + \chi \mathcal{P}_m x') = 0, \quad (\text{IV.28})$$

$$\partial_u(\mathcal{P}_X x' + \chi \mathcal{P}_m b_X') = 0, \quad (\text{IV.29})$$

$$\partial_u(\mathcal{P}_\omega \psi_I') + \mathcal{M} b_X^2 \psi_I = 0. \quad (\text{IV.30})$$

The important point is the index structure. The hidden field strength is purely electric,

$$X_{ut} = x'(u), \quad X_{x_i P} = 0 \quad (i = 1, \dots, d). \quad (\text{IV.31})$$

For a two-form whose only nonzero component is  $ut$ , the mixed-index stress tensor in any boundary spatial direction has no “direct” term  $X^{x_i P} X_{x_i P}$ . The only contribution to  $T^{x_i}_{x_i}$  is the trace term, so

$$T^{x_i}_{x_i}[X] = -\frac{1}{4} Z_X(\phi) X_{MN} X^{MN}, \quad i = 1, 2, \dots, d. \quad (\text{IV.32})$$

This expression is independent of  $i$ . The mixing term has the same property. It is made from  $G_{ut}^3 X^{ut}$ , again with no boundary spatial index, and gives

$$T^{x_i}_{x_i}[G^3 X] = -\frac{1}{2} \chi Z_m(\phi) G_{ut}^3 X^{ut}, \quad i = 1, 2, \dots, d. \quad (\text{IV.33})$$

Therefore the hidden Abelian electric sector cancels in the traceless spatial combination:

$$(T^{x_1}_{x_1} - T^{x_2}_{x_2})_{X, G^3 X} = 0. \quad (\text{IV.34})$$

After this cancellation, the extra Case-I source in Eq. (IV.12) is zero:

$$S_{\text{aniso}}^{\text{I}}(u) - S_{\text{aniso}}^{\text{vis}}(u) = 0. \quad (\text{IV.35})$$

Therefore the difference  $A_2^{\text{I}} - A_2^{\text{vis}}$  obeys the homogeneous Einstein equation with zero boundary source and regular horizon behavior. It follows that

$$A_2^{\text{I}}(u) = A_2^{\text{vis}}(u), \quad \mathcal{O}_{12}^{(2), \text{I}}(W) = \mathcal{O}_{12}^{(2), \text{vis}}(W) \quad (D = 4, 5). \quad (\text{IV.36})$$

With the relative response

$$\Delta_{12}^X \equiv \frac{\mathcal{O}_{12}^{(2), X} - \mathcal{O}_{12}^{(2), \text{vis}}}{|\mathcal{O}_{12}^{(2), \text{vis}}|}, \quad (\text{IV.37})$$

this gives  $\Delta_{12}^{\text{I}} = 0$ . Thus Case I is null in the orientation difference for a concrete reason: the new hidden terms are temporal electric terms, temporal electric stress is spatially isotropic, the traceless metric equation receives no new source, and the two oriented RT areas shift equally.

Case II is different because the hidden sector contains its own spatial non-Abelian vector. We introduce the hidden field strengths explicitly because they show which hidden terms enter the same magnetic-minus-electric source as the visible  $p$ -wave field. With  $C_t^3 = \eta(u)$  and  $C_{x_1}^1 = \omega_d(u)$ ,

$$H_{ut}^3 = \eta'(u), \quad H_{ux_1}^1 = \omega'_d(u), \quad H_{tx_1}^2 = -\eta(u)\omega_d(u). \quad (\text{IV.38})$$

The first component,  $H_{ut}^3$ , is a temporal electric background. The second,  $H_{ux_1}^1$ , is the hidden radial magnetic component. The third,  $H_{tx_1}^2$ , is the hidden non-Abelian electric component generated by the commutator of the temporal and spatial fields. Therefore the anisotropic source is obtained by adding the visible terms, the hidden terms, and the mixed terms from  $G_{MN}^a H^{aMN}$ :

$$S_{\text{aniso}}^{\text{II}}(u) = \mathcal{P}_\omega (\omega'_v{}^2 + \alpha_{\text{dm}} \omega'_v \omega'_d + \omega'_d{}^2)$$

$$- \mathcal{M} (b^2 \omega_v^2 + \alpha_{\text{dm}} b \eta \omega_v \omega_d + \eta^2 \omega_d^2). \quad (\text{IV.39})$$

The first line is the  $ux_1$  magnetic part. The second line is the  $tx_1$  electric part. The cross terms are not optional: they are the stress-tensor imprint of the kinetic mixing.

In the minimal ensemble with no independent hidden chemical potential, the temporal equations give

$$\eta(u) = -\frac{\alpha_{\text{dm}}}{2} b(u). \quad (\text{IV.40})$$

At the critical point, the coupled visible and hidden vector equations admit a constant-ratio zero mode,

$$\omega_d(u) = \gamma \omega_v(u), \quad (\text{IV.41})$$

where  $\gamma$  is fixed by Eq. (III.13). The magnetic part of Eq. (IV.39) is then straightforward:

$$\omega_v'^2 + \alpha_{\text{dm}} \omega_v' \omega_d' + \omega_d'^2 = (1 + \alpha_{\text{dm}} \gamma + \gamma^2) \omega_v'^2. \quad (\text{IV.42})$$

We define this factor as

$$\mathcal{R}_{\text{HEE}}^{\text{II}} = 1 + \alpha_{\text{dm}} \gamma + \gamma^2. \quad (\text{IV.43})$$

The electric part needs one extra step. If one keeps  $b(u)$  fixed and only inserts  $\eta = -\alpha_{\text{dm}} b/2$  and  $\omega_d = \gamma \omega_v$ , then the electric bracket becomes

$$b^2 \omega_v^2 + \alpha_{\text{dm}} b \eta \omega_v \omega_d + \eta^2 \omega_d^2 = f_E b^2 \omega_v^2, \quad f_E = 1 - \frac{\alpha_{\text{dm}}^2}{2} \gamma + \frac{\alpha_{\text{dm}}^2}{4} \gamma^2. \quad (\text{IV.44})$$

This is the step at which the calculation is most easily misread. The Case-II critical mode is not compared at a fixed visible electric amplitude. It is evaluated at its own critical point. The visible component of the coupled zero-mode equation is

$$\partial_u (\mathcal{P}_\omega \omega_v') + \lambda_{\text{II}} \mathcal{M} b^2 \omega_v = 0, \quad \lambda_{\text{II}} = \frac{1 - \frac{\alpha_{\text{dm}}^2}{4} \gamma}{1 + \frac{\alpha_{\text{dm}}}{2} \gamma}. \quad (\text{IV.45})$$

The visible reference equation is

$$\partial_u (\mathcal{P}_\omega \psi_{\text{vis}}') + \mathcal{M} b_{\text{vis}}^2 \psi_{\text{vis}} = 0. \quad (\text{IV.46})$$

For the Case-II zero mode to have the same radial shape as the visible zero mode, the coefficients multiplying  $\mathcal{M}$  in these two equations must agree. Hence

$$\lambda_{\text{II}} b_{\text{II}}(u)^2 = b_{\text{vis}}(u)^2, \quad b_{\text{II}}(u)^2 = \frac{b_{\text{vis}}(u)^2}{\lambda_{\text{II}}}. \quad (\text{IV.47})$$

Since the normal electric solution is proportional to the boundary chemical potential, this is equivalently

$$\frac{\mu_c^{\text{II}}}{\mu_c^{\text{vis}}} = \lambda_{\text{II}}^{-1/2}. \quad (\text{IV.48})$$

Thus the electric part of the Case-II stress carries the factor  $f_E/\lambda_{\text{II}}$ , not  $f_E$ . The constant-ratio equation for  $\gamma$  then gives

$$f_E - \lambda_{\text{II}} \mathcal{R}_{\text{HEE}}^{\text{II}} = \frac{2\gamma}{2 + \alpha_{\text{dm}}\gamma} \left[ \frac{\alpha_{\text{dm}}^2}{4} \left( 1 + \frac{\alpha_{\text{dm}}}{2} \right) \gamma^2 - \left( 1 - \frac{\alpha_{\text{dm}}^2}{4} \right) \gamma - \left( \frac{\alpha_{\text{dm}}}{2} + \frac{\alpha_{\text{dm}}^2}{4} \right) \right] = 0. \quad (\text{IV.49})$$

The bracket is exactly Eq. (III.13). Therefore

$$\frac{f_E}{\lambda_{\text{II}}} = \mathcal{R}_{\text{HEE}}^{\text{II}}, \quad (\text{IV.50})$$

and the magnetic and electric parts are multiplied by the same factor. The full local source factorizes pointwise:

$$S_{\text{aniso}}^{\text{II}}(u) = \mathcal{R}_{\text{HEE}}^{\text{II}} S_{\text{aniso}}^{\text{vis}}(u). \quad (\text{IV.51})$$

This is why Case II is scale-independent. The multiplier depends only on  $\alpha_{\text{dm}}$  through  $\gamma$ ; it does not depend on  $D$ ,  $\theta$ ,  $z$ ,  $W$ , or on the RT kernel.

Case III-a contains a scalar, but the scalar is a singlet depending only on  $u$ . The scalar equation is Eq. (II.80), and the mass portal changes the vector critical equation to

$$\partial_u(\mathcal{P}_\omega \psi'_a) + \mathcal{M} b_0^2 \psi_a - U_\Phi(u) \psi_a = 0, \quad U_\Phi(u) = 2\alpha_{\text{dm}}^2 \lambda_{\Phi B} \sqrt{-g} g^{x_1 x_1} \Phi^2. \quad (\text{IV.52})$$

The scalar itself carries no boundary spatial index. Since  $\partial_{x_i} \Phi = 0$ , its spatial stress is proportional to  $\delta^i_j$ :

$$T^{x_i}_{x_j}[\Phi] = \delta^i_j \frac{1}{2} \left[ -g^{uu} \Phi'^2 - m_\Phi^2 e^{\lambda_{\Phi\phi}\phi} \Phi^2 \right], \quad i, j = 1, \dots, d, \quad (\text{IV.53})$$

and therefore

$$(T^{x_1}_{x_1} - T^{x_2}_{x_2})_\Phi = 0. \quad (\text{IV.54})$$

The mass portal in Eq. (IV.52) is used here as an isotropic radial cost in the critical operator. It can change  $\mu_c$ , because it changes the eigenvalue problem for forming the vector mode, but it does not introduce a hidden spatial vector or a gauge-kinetic reweighting of the anisotropic Yang–Mills stress. The extra scalar contribution to the traceless Einstein equation is therefore zero:

$$S_{\text{aniso}}^{\text{IIIa}}(u) - S_{\text{aniso}}^{\text{vis}}(u) = 0. \quad (\text{IV.55})$$

As in Case I, the difference  $A_2^{\text{IIIa}} - A_2^{\text{vis}}$  then solves the homogeneous version of Eq. (IV.12) with the same boundary and horizon conditions. Hence

$$A_2^{\text{IIIa}}(u) = A_2^{\text{vis}}(u), \quad \mathcal{O}_{12}^{(2),\text{IIIa}}(W) = \mathcal{O}_{12}^{(2),\text{vis}}(W), \quad \Delta_{12}^{\text{IIIa}} = 0 \quad (D = 4, 5). \quad (\text{IV.56})$$

This is the sense in which Case III-a is a null channel for  $\mathcal{O}_{12}^{(2)}$ : it changes the scalar cost of forming the vector mode, but it does not supply a new traceless source for the metric perturbation measured by the orientation difference.

Finally, Case III-b inserts the same scalar solution into the Yang–Mills kinetic operator before solving the temporal and spatial equations:

$$\partial_u[Z_{\text{dm}}(\Phi)\mathcal{P}_b b'_Z] = 0, \quad (\text{IV.57})$$

$$\partial_u[Z_{\text{dm}}(\Phi)\mathcal{P}_\omega \psi'_Z] + Z_{\text{dm}}(\Phi)\mathcal{M}b_Z^2 \psi_Z = 0. \quad (\text{IV.58})$$

Only after these two radial equations are solved do we build the metric source, namely

$$S_{\text{aniso}}^{\text{IIIb}}(u) = Z_{\text{dm}}(\Phi(u)) \left[ u^{d\theta+d+3z-3} N_0(u) \psi'_Z(u)^2 - u^{d\theta+z+d-5} \frac{b_Z(u)^2 \psi_Z(u)^2}{N_0(u)} \right]. \quad (\text{IV.59})$$

Equation (IV.59) is the radial source that enters the first variation of the RT area. For this channel we keep two expansions separate. The first expansion is the linear response to the scalar gauge-kinetic portal, not a short-width expansion. We write

$$Z_{\text{dm}}(\Phi) = 1 + \lambda_Z \Phi^2 + O(\lambda_Z^2), \quad |\lambda_Z \Phi^2| \ll 1, \quad (\text{IV.60})$$

where  $\lambda_Z$  is the dimensionless coefficient multiplying the scalar correction  $\Phi^2 G_{MN}^a G^{aMN}$  in the visible Yang–Mills kinetic term. It is a portal coupling, not a geometric small-width parameter. At fixed HSV background, the visible normal electric field and visible critical vector mode are denoted by  $b_0(u)$  and  $\psi_{\text{vis}}(u)$ . To first order in  $\lambda_Z$ ,

$$b_Z(u) = b_0(u) + \lambda_Z b_1(u) + O(\lambda_Z^2), \quad \psi_Z(u) = \psi_{\text{vis}}(u) + \lambda_Z \psi_1(u) + O(\lambda_Z^2). \quad (\text{IV.61})$$

Here  $b_1$  and  $\psi_1$  are the first-order changes induced by the same gauge-kinetic factor  $Z_{\text{dm}}$ . Linearizing the Case-III-b radial equations gives

$$\partial_u(\mathcal{P}_b b'_1) = -\partial_u(\mathcal{P}_b \Phi^2 b'_0), \quad (\text{IV.62})$$

$$[\partial_u(\mathcal{P}_\omega \partial_u) + \mathcal{M}b_0^2] \psi_1 = -\partial_u(\mathcal{P}_\omega \Phi^2 \psi'_{\text{vis}}) - \mathcal{M}\Phi^2 b_0^2 \psi_{\text{vis}} - 2\mathcal{M}b_0 b_1 \psi_{\text{vis}}. \quad (\text{IV.63})$$

Thus the scalar does not merely multiply the final HEE observable; it perturbs the electric field and the vector zero mode before the metric response is constructed.

Substituting Eqs. (IV.60) and (IV.61) into Eq. (IV.59) gives

$$S_{\text{aniso}}^{\text{IIIb}}(u) - S_{\text{aniso}}^{\text{vis}}(u) = \lambda_Z \delta S_\Phi(u) + O(\lambda_Z^2), \quad (\text{IV.64})$$

$$\delta S_\Phi(u) = \Phi(u)^2 S_{\text{aniso}}^{\text{vis}}(u) + 2\mathcal{P}_\omega \psi'_{\text{vis}} \psi'_1 - 2\mathcal{M}b_0 b_1 \psi_{\text{vis}}^2 - 2\mathcal{M}b_0^2 \psi_{\text{vis}} \psi_1.$$

The first term is the direct kinetic reweighting. The other terms are not higher order:  $b_1$  and  $\psi_1$  are themselves first order in the same deformation, as shown in Eqs. (IV.62) and (IV.63). Therefore the absolute coefficient of the Case-III-b HEE response is not obtained by replacing  $S_{\text{aniso}}^{\text{vis}}$  pointwise by  $\Phi^2 S_{\text{aniso}}^{\text{vis}}$ .

The second expansion is the short-width expansion of the RT surface. This is independent of the smallness of  $\lambda_Z$ . For a thin interval or strip, the turning point satisfies  $u_*(W) \sim W^{-1}$ , so the RT surface remains in the UV region. The scalar equation has two UV falloffs,

$$\Phi(u) = \Phi_- u^{-\Delta_-} + \Phi_+ u^{-\Delta_+} + \dots, \quad \Delta_- + \Delta_+ = d(1 + \theta) + z. \quad (\text{IV.65})$$

In the parametrization used in the scalar BVP, one root is called  $\Delta_\Phi$  and the other is  $d(1 + \theta) + z - \Delta_\Phi$ . The exponent controlling the leading UV term is therefore

$$\Delta_{\text{UV}} = \min\{\Delta_\Phi, d(1 + \theta) + z - \Delta_\Phi\}, \quad (\text{IV.66})$$

unless the coefficient of the slower falloff is set to zero by the boundary condition. For the sourced scalar solutions used here this leading coefficient is nonzero. We denote it by  $\Phi_{\text{src}}$ , so that

$$\Phi(u) = \Phi_{\text{src}} u^{-\Delta_{\text{UV}}} + \text{subleading powers of } u^{-1}. \quad (\text{IV.67})$$

The coefficient  $\Phi_{\text{src}}$  is the source amplitude of the leading UV falloff; changing it rescales the Case-III-b response but does not change the width exponent.

The first variation of the RT area has the form

$$\delta S_{\text{RT}}^{\text{IIIb}}(W) = \lambda_Z \int_{u_*(W)}^{\infty} du K_{\text{RT}}^{(D)}(u; u_*) \delta S_\Phi(u) + O(\lambda_Z^2), \quad (\text{IV.68})$$

where  $K_{\text{RT}}^{(D)}$  is the interval or strip first-variation kernel. Setting  $u = u_* y$ , the HSV powers from the visible stress and from the RT kernel factor out in the same way as in the visible response. The additional scalar dependence contributes

$$\Phi^2(u_* y) = \Phi_{\text{src}}^2 u_*^{-2\Delta_{\text{UV}}} y^{-2\Delta_{\text{UV}}} + \text{subleading powers}. \quad (\text{IV.69})$$

The remaining integral over  $y \geq 1$  is finite. Since  $u_*(W) \sim W^{-1}$ , the leading short-width behavior is

$$\Delta_{12}^{\text{IIIb}}(W) = \text{finite coefficient} \times \lambda_Z \Phi_{\text{src}}^2 W^{2\Delta_{\text{UV}}} + \text{subleading powers in } W + O(\lambda_Z^2), \quad (D = 4, 5). \quad (\text{IV.70})$$

For  $D = 3$ , the same UV argument applies to the interval response rather than to a strip orientation difference. The finite coefficient in Eq. (IV.70) depends on the RT kernel moment and on  $b_1, \psi_1$ . We do not use that coefficient as a physical prediction. The normalization-independent information used in the figures is the sign, the absence or presence of width dependence, and the exponent  $2\Delta_{\text{UV}}$ .

The mechanism behind the scale-resolved diagnostic can now be summarized without referring to the figures. Combining the linearized Einstein equation for  $A_2$  with the RT first variation gives a linear map from the local anisotropic source to the orientation observable. Schematically,

$$\mathcal{O}_{12}^{(2),X}(W) - \mathcal{O}_{12}^{(2),\text{vis}}(W) = \int_1^\infty du \mathcal{K}_{12}^{(D)}(u; W) [S_{\text{aniso}}^X(u) - S_{\text{aniso}}^{\text{vis}}(u)], \quad (\text{IV.71})$$

where  $\mathcal{K}_{12}^{(D)}(u; W)$  denotes the finite kernel obtained by solving Eq. (IV.12) and inserting the result into Eq. (IV.13). Its detailed normalization is not important for the classification below; its radial support moves with the strip width  $W$ .

Equation (IV.71) explains the separation of dark-sector responses. In Cases I and III-a the bracket in Eq. (IV.71) vanishes at leading order for  $D = 4, 5$ , so the orientation difference filters out those isotropic hidden sources. In Case II,  $S_{\text{aniso}}^{\text{II}} = \mathcal{R}_{\text{HEE}}^{\text{II}} S_{\text{aniso}}^{\text{vis}}$ . The kernel in Eq. (IV.71) may depend on  $W$ , but it acts on the same radial function as in the visible theory. Hence the ratio to the visible answer is a constant: Case II is a scale-independent hidden-current renormalization of the anisotropic current response.

Case III-b is different in the precise holographic-RG sense. The radial coordinate labels the energy scale of the boundary effective theory, and the strip width selects a radial depth: small  $W$  stays near the UV boundary, while larger  $W$  gives more weight to the interior. A constant multiplication of  $S_{\text{aniso}}^{\text{vis}}$  therefore looks the same at every width. By contrast,  $Z_{\text{dm}}(\Phi(u))$ ,  $b_1(u)$ , and  $\psi_1(u)$  vary along the radial direction, so the hidden deformation changes from scale to scale. Changing  $W$  changes which part of that radial deformation is weighted by the RT surface, and the relative response runs with  $W$ . The short-width limit is governed by Eq. (IV.70); hence the normalization-independent claims are the sign, the width dependence, and the  $W^{2\Delta_{\text{UV}}}$  exponent, not the absolute finite-width coefficient. We use this operationally as an entanglement RG probe: it distinguishes a constant current normalization from a radially dependent hidden deformation without claiming to compute a separate UV beta function.

The constants  $k_4$  and  $k_5$  fix the normalization of the metric function  $A_2$ . We determine them by matching the numerical response to the closed visible solutions at the two analytic reference backgrounds. This convention reproduces the visible  $D = 4$  and  $D = 5$  metric solutions used in the RT calculation. A redefinition of  $A_2$  changes the source coefficient and the RT insertion together; the gauge-kinetic-portal susceptibility below is a dark-to-visible ratio within one fixed dimension, so this common normalization cancels. We therefore do not interpret the absolute sign or normalization of  $k_D$  as an additional cross-dimensional result.

We can also check the first law to fix the normalization of the leading RT response. For a small interval, strip, or slab region  $\mathcal{A}$ , the relevant relation is the standard small-subregion entanglement first law,

$$\Delta E_{\mathcal{A}} = T_{\text{ent}} \Delta S_{\mathcal{A}}. \quad (\text{IV.72})$$

Here  $\Delta E_{\mathcal{A}}$  is obtained by integrating the homogeneous energy density over the same boundary region, including the regulated transverse volume for strip and slab regions. In the controlled  $z = 1$  normalization used for the first-law check, that energy density is read from the normalizable mass coefficient of the metric response; no additional thermodynamic parameter is introduced in the figure analysis.

For homogeneous small subregions the entanglement temperature scales as  $T_{\text{ent}} \sim 1/\ell$ . The appendix plots therefore display the leading undeformed entropy, its leading small-subregion variation, the dimensionless product  $T_{\text{ent}}\ell$ , and the difference between the two sides of Eq. (IV.72). These plots are kept in the appendix because they validate the RT normalization rather than introducing a separate dark-sector mechanism. Extending this thermodynamic interpretation to generic HSV/Lifshitz exponents would require the full holographic stress tensor

and counterterm scheme.

#### IV.B. How hidden sectors enter the anisotropic RT response

The orientation observable removes isotropic shifts. The two strip entropies are decomposed as

$$S_{\parallel} = S_{\text{iso}}^{(0)} - \frac{1}{2}\delta^2\epsilon^2\mathcal{O}_{12}^{(2)} + O(\epsilon^4), \quad S_{\perp} = S_{\text{iso}}^{(0)} + \frac{1}{2}\delta^2\epsilon^2\mathcal{O}_{12}^{(2)} + O(\epsilon^4). \quad (\text{IV.73})$$

The leading term is the undeformed HSV strip entropy. For a strip with turning point  $u_*$ , with  $p = 2d(1 + \theta)$  and  $q = d(1 + \theta) - 1$ , the finite part is

$$S_{\text{iso}}^{(0)} = 2 \left[ \int_{u_*}^{\infty} du \left( \frac{u^{q-1}}{\sqrt{N_0(u)}\sqrt{1 - (u_*/u)^p}} - u^{q-1} \right) - \frac{u_*^q}{q} \right], \quad (\text{IV.74})$$

with the usual logarithmic replacement for  $q = 0$ .

Equation (IV.73) explains why Case I and Case III-a are null in  $\mathcal{O}_{12}^{(2)}$ : they are isotropic in the leading orientation channel and hence shift  $S_{\parallel}$  and  $S_{\perp}$  equally. Case II with  $\mu_X = 0$  rescales the same anisotropic source. In the corrected coupled-channel treatment this scale-independent response is

$$\Delta S_{\text{int}}^{(2)}(\alpha_{\text{dm}}) = \mathcal{R}_{\text{HEE}}^{\text{II}}(\alpha_{\text{dm}}) \Delta S_{\text{int}}^{(2)}(0), \quad \mathcal{O}_{12}^{(2)}(\alpha_{\text{dm}}) = \mathcal{R}_{\text{HEE}}^{\text{II}}(\alpha_{\text{dm}}) \mathcal{O}_{12}^{(2)}(0), \quad (\text{IV.75})$$

where  $\mathcal{R}_{\text{HEE}}^{\text{II}} = 1 + \alpha_{\text{dm}}\gamma + \gamma^2$  and  $\gamma$  is the coupled visible-hidden eigenvector ratio defined in Sec. III.C 2 a. Case III-b is not a constant-rescaling case: the scalar-dependent kinetic factor changes the radial weights of the anisotropic source, so the HEE response must be computed as a radial-shape effect.

#### IV.C. Gauge-kinetic-portal susceptibility as a linear response coefficient

The finite-amplitude portal figures use representative values chosen to make the scale dependence visible. They should not be confused with a phenomenologically small dark-photon kinetic-mixing regime; the linear response coefficients are extracted separately from the small-coupling window. Unless otherwise stated, the Case-III-b response figures use a source-normalized scalar BVP with  $\Delta_{\Phi} = 1.10$ , reference width  $W_{\text{ref}} = 0.10$ , and leading UV source amplitude  $\Phi_{\text{src}} = 0.4$ . The value  $\Delta_{\Phi} = 1.10$  lies away from the two-falloff degeneracy, so the short-width exponent is stable, and  $W_{\text{ref}} = 0.10$  keeps the RT surface in the UV region where Eq. (IV.70) applies. Since the scalar BVP is linear in  $\Phi_{\text{src}}$  and the leading gauge-kinetic-portal response is quadratic in  $\Phi$ , changing  $\Phi_{\text{src}}$  rescales the plotted Case-III-b magnitude but does not change the sign or the exponent.

We use the word susceptibility in the standard linear-response sense: it is the derivative of an observable with respect to the coefficient of an external deformation, evaluated at zero

deformation. Here the deformation is the coefficient  $\lambda_Z$  multiplying  $\Phi^2$  in  $Z_{\text{dm}}(\Phi) = 1 + \lambda_Z \Phi^2 + O(\lambda_Z^2)$ . For the strip-difference observable in  $D = 4, 5$ ,

$$\chi_{\text{kin}}^{\text{strip}}(W) = \frac{\partial}{\partial \lambda_Z} \left[ \frac{\mathcal{O}_{12}^{(2)}(W; \lambda_Z)}{\mathcal{O}_{12}^{(2)}(W; 0)} - 1 \right] \Bigg|_{\lambda_Z=0}. \quad (\text{IV.76})$$

The derivative is taken after recomputing both the normal-phase temporal component and the vector zero mode with the same kinetic factor. Therefore  $\chi_{\text{kin}}^{\text{strip}}$  is not just the explicit multiplier  $\Phi^2$ ; it is the net first-order change of the strip anisotropy after  $b_0$ ,  $\omega_1$ , and the traceless Yang–Mills source all respond to the portal. A constant hidden-current rescaling gives no width-dependent coefficient, and an isotropic dark source gives zero in the strip difference. This is why the gauge-kinetic portal is the natural channel for a running HEE response, while the Case-II scaling law remains a scale-independent hidden-current mixing model.

The same construction could be applied to the  $D = 3$  interval coefficient, but that quantity is not the same strip-difference observable. We therefore reserve  $\chi_{\text{kin}}^{\text{strip}}$  for the  $D = 4, 5$  strip comparison and report the interval response separately.

#### IV.D. Nonlinear condensate and extraction of $\langle O \rangle$

The order-parameter figures use  $\langle O \rangle$ , where

$$O \equiv J_{x_1}^1. \quad (\text{IV.77})$$

This is the boundary vector-current component dual to the normalizable part of the visible spatial gauge field  $B_{x_1}^1$ . It is not the dark scalar  $\Phi$ . A nonzero  $\langle O \rangle$  means that the visible  $SU(2)$  current has condensed along  $x_1$ , breaking spatial rotations.

The expectation value is extracted from the finite-amplitude source-free solution. We write

$$B = \varphi(u)\tau^3 dt + w(u)\tau^1 dx_1, \quad (\text{IV.78})$$

where  $\varphi$  is the temporal component and  $w$  is the nonlinear vector solution. The probe equations are

$$(u^A N_0 w')' + \frac{u^r}{N_0} \varphi^2 w = 0, \quad (\text{IV.79})$$

$$(u^M \varphi')' - \frac{u^r}{N_0} \varphi w^2 = 0, \quad (\text{IV.80})$$

with

$$A = d\theta + d + 3z - 3, \quad M = d\theta + z + d - 1, \quad r = d(1 + \theta) + z - 5. \quad (\text{IV.81})$$

The horizon amplitude  $w(1) = w_{\text{hor}}$  is used as a continuation parameter to avoid the trivial solution  $w \equiv 0$ .

At the boundary,

$$\varphi(u) = \mu - \rho u^{-m} + \dots, \quad m = n_h - 2, \quad (\text{IV.82})$$

$$w(u) = w_{\text{src}} + w_{\text{vev}} u^{-\Delta_O} + \dots, \quad \Delta_O = d\theta + d + 3z - 4. \quad (\text{IV.83})$$

The source-free condition is  $w_{\text{src}} = 0$ , and the normalizable coefficient gives

$$\langle O \rangle = \mathcal{N}_O w_{\text{vev}}. \quad (\text{IV.84})$$

The constant  $\mathcal{N}_O$  is conventional, so the figures emphasize the critical point, the scaling with  $\mu - \mu_c$ , and the visible/dark displacement rather than an absolute vertical normalization.

Near the critical point,

$$\mu = \mu_c + \mu_2 w_{\text{hor}}^2 + O(w_{\text{hor}}^4), \quad \langle O \rangle = \mathcal{C} w_{\text{hor}} + O(w_{\text{hor}}^3), \quad (\text{IV.85})$$

so  $\langle O \rangle \propto (\mu - \mu_c)^{1/2}$ . For the minimal hidden  $SU(2)$  family, the nonlinear solution family should be organized around the corrected coupled visible–hidden critical mode. The condensate still turns on with the mean-field exponent,

$$\langle O \rangle \propto (\mu - \mu_c)^{1/2}, \quad (\text{IV.86})$$

but the critical reference line for  $\mu_c$  is the coupled-mode value in Eq. (III.14). Scalar and gauge-kinetic portals are not inferred from this curve; they require their own finite-amplitude scalar–vector systems.

## V. RESULTS

The visible HSV p-wave system provides the baseline against which all dark-sector effects are measured. Figure 1 shows this baseline only through dark-minus-visible comparisons, so that the normalization and the degeneracies are visible in the same plot. The  $z = 2$  slice is a representative  $\theta$ -scan, not an assumption of  $z$ -independence for the scalar portal. The point of this figure is already visible at the level of ratios: the leading classification changes little when the HSV exponents are varied. The null cases remain null, and the hidden-current factor is algebraic. The only displayed channel with genuine residual  $(\theta, z)$  dependence is Case III-b, and that dependence is shown explicitly in Fig. 2. In each bulk dimension  $D = 3, 4, 5$ , the figure displays the critical-scale ratio  $\mu_c^X / \mu_c^{\text{vis}}$  and the response ratio appropriate to the dimension. Case I and Case III-a are drawn as separate null-case curves even when they sit on top of the visible line.

The main selection rule is displayed in Fig. 2. The relative panels are used deliberately to avoid the ill-conditioned direct-subtraction ratios in the raw Case-III-b  $O_{12}$  table. Here the visible-sector  $O_{12}$  construction is used as a baseline rather than as the final result: the dark-sector information is carried by the deviation from, or degeneracy with, that baseline. The

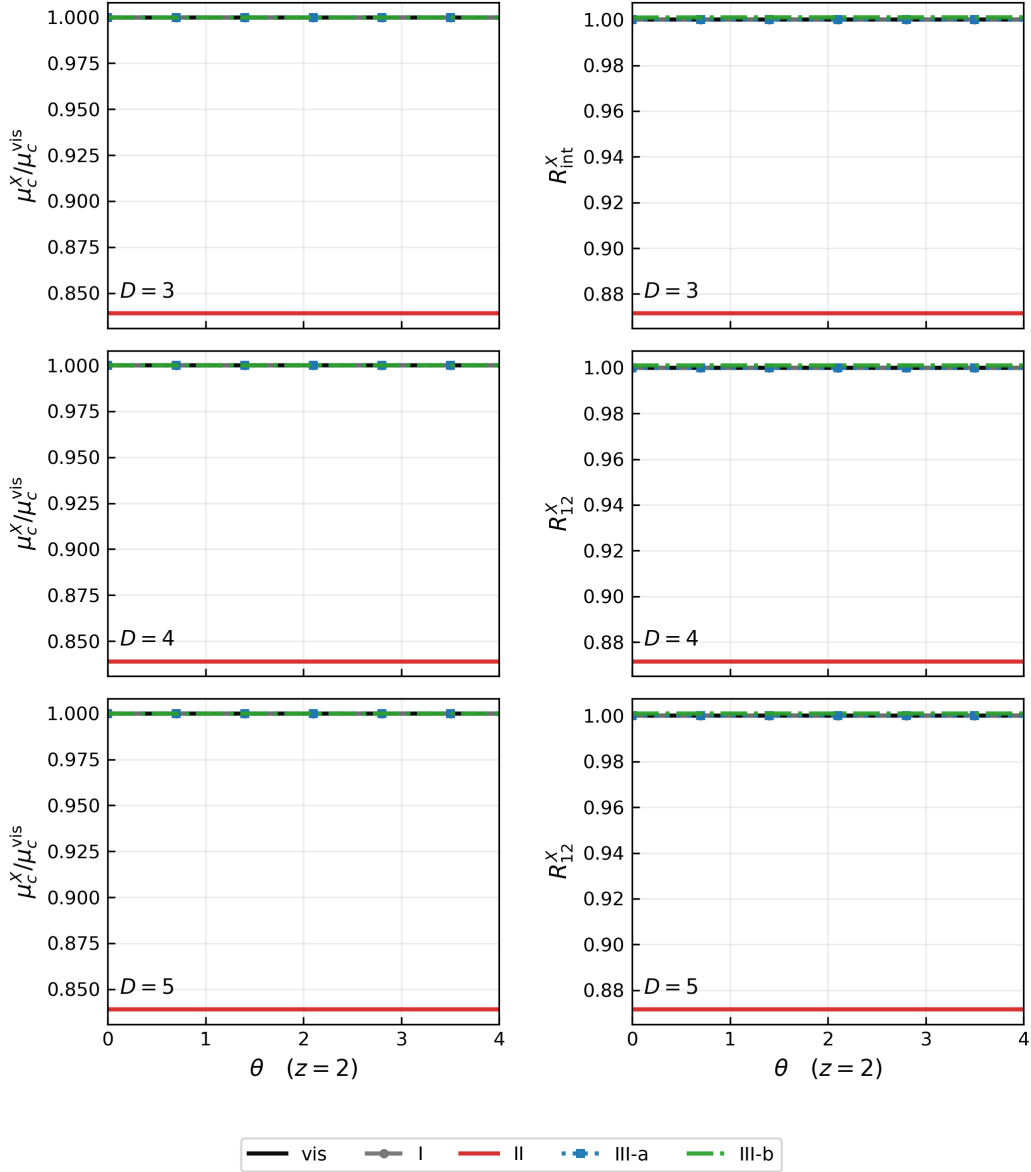


FIG. 1. Representative dark-visible comparison at fixed  $z = 2$ . Rows are  $D = 3, 4, 5$ . The left column shows the critical-scale ratio relative to the visible sector; in this leading-order scan Case III-b has  $\mu_c^{\text{IIIb}}/\mu_c^{\text{vis}} = 1$ , so it lies on the visible/null-case line. The right column shows the response ratio:  $R_{\text{int}}^X$  for the  $D = 3$  interval coefficient and  $R_{12}^X$  for the  $D = 4, 5$  strip-orientation difference. The visible, Case I, and Case III-a curves are drawn with separate line styles even where they coincide. Case II uses the coupled hidden-current factor, whereas Case III-b uses the well-conditioned perturbative scalar-BVP ratio rather than the unstable direct subtraction of two nearly equal strip areas. The complementary  $z$ -dependence is shown in Fig. 2.

orientation difference  $O_{12} = S_{\perp} - S_{\parallel}$  projects out channels that do not generate a traceless anisotropic source. Thus Case I and the isotropic scalar mass portal, Case III-a, are null cases at leading order: they coincide with the visible baseline in the orientation-difference observable even though they can shift scalar thermodynamic quantities. Case II survives as a scale-independent current-mixing factor, because the visible and hidden vector channels carry the same radial weights. Case III-b survives differently, because  $Z_{\text{dm}}(\Phi(u))$  changes the radial weight of the visible Yang–Mills operator. The displayed scan uses two dense orthogonal slices through the  $(\theta, z)$  plane,  $z = 2$  for the  $\theta$ -scan and  $\theta = 1$  for the  $z$ -scan. The scan shows that the qualitative separation is insensitive to the detailed point chosen in the HSV family: changing  $\theta$  and  $z$  changes the visible normalization, the RT weight, and the scalar falloff, but it does not mix the null, constant, and width-running classes. The only residual  $(\theta, z)$  structure belongs to Case III-b. For the displayed scalar normalization it has a range-over-min spread of about 13.5% in the  $D = 3$  interval row, but remains below the percent level in the  $D = 4, 5$  strip-anisotropy rows.

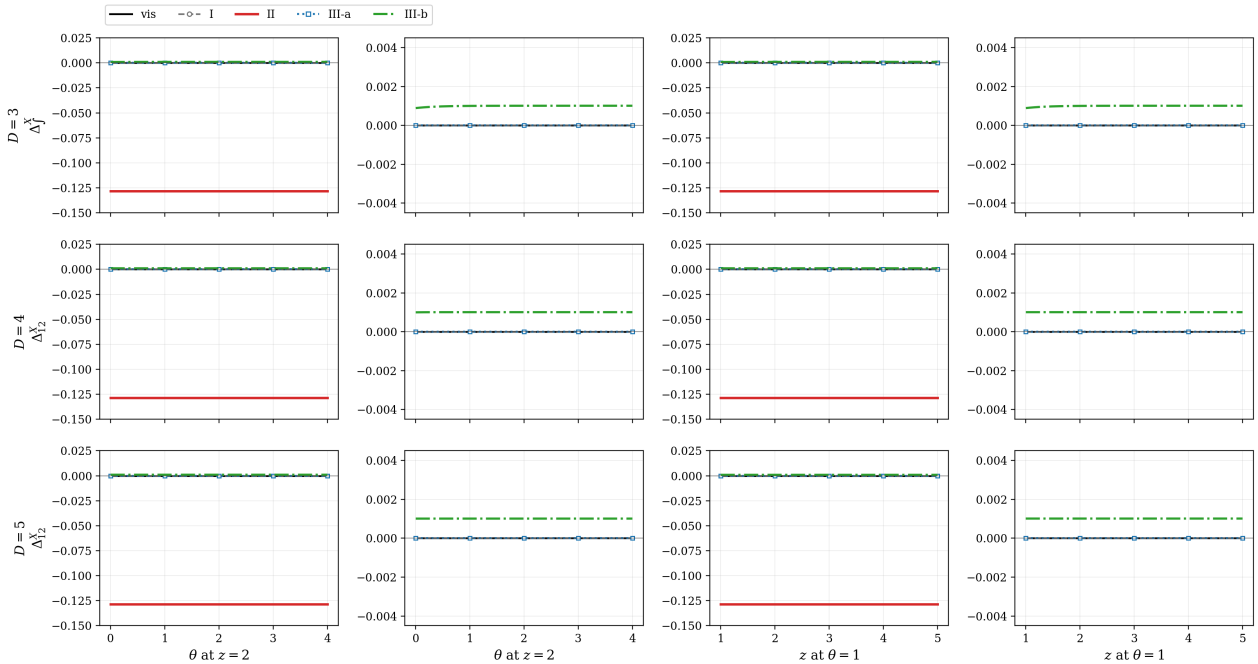


FIG. 2. Central relative-response scan. Rows are  $D = 3, 4, 5$ . The four columns show, from left to right, a full-range  $\theta$ -scan at fixed  $z = 2$ , a near-zero zoom of the same  $\theta$ -scan, a full-range  $z$ -scan at fixed  $\theta = 1$ , and a near-zero zoom of the same  $z$ -scan. The plotted quantity is  $\Delta_{\text{int}}^X$  for the  $D = 3$  interval coefficient and  $\Delta_{12}^X = (O_{12}^{(2),X} - O_{12}^{(2),\text{vis}})/|O_{12}^{(2),\text{vis}}|$  for  $D = 4, 5$ . Null cases are overplotted on the zero line with distinct line styles. Case III-b is computed from the perturbative short-width response in Eq. (IV.70), avoiding the ill-conditioned direct subtraction of nearly equal RT areas.

### V.A. Case II: hidden-current hybridization and competing vector order

The lowest Case-II critical mode is a visible–hidden two-component vector eigenmode. Case II deserves a separate figure because, unlike the scalar portal, its constant- $\gamma$  solution uses the same radial weight in the visible and hidden vector channels. The HSV exponents enter the common visible operator, but they cancel out of the ratios that compare the two mixed current components. Therefore  $\mu_c^{\text{II}}/\mu_c^{\text{vis}}$ ,  $\mathcal{R}_{12}^{\text{II}}$ , and  $f_d$  are algebraic functions of  $\alpha_{\text{dm}}$  and are independent of  $D$ ,  $\theta$ ,  $z$ , and  $W$  in the minimal ensemble. Repeating a  $(\theta, z)$  scan for these ratios would reproduce the same curves, so Fig. 3 displays the algebraic hybridization itself. The hidden fraction

$$f_d = \frac{\gamma^2}{1 + \gamma^2} \quad (\text{V.1})$$

quantifies how much of the critical instability resides in the hidden spatial component. In the minimal ensemble used here  $f_d$  grows from zero to  $f_d \simeq 0.42$  at  $\alpha_{\text{dm}} = 1.2$ . Thus the instability remains visible enough to be read as a p-wave transition, but it is no longer a merely visible instability with a small normalization error; it is a strongly hybridized visible–hidden vector mode. This competing-vector-order hybridization is specific to the anisotropic p-wave channel and would be invisible in an isotropic scalar response.

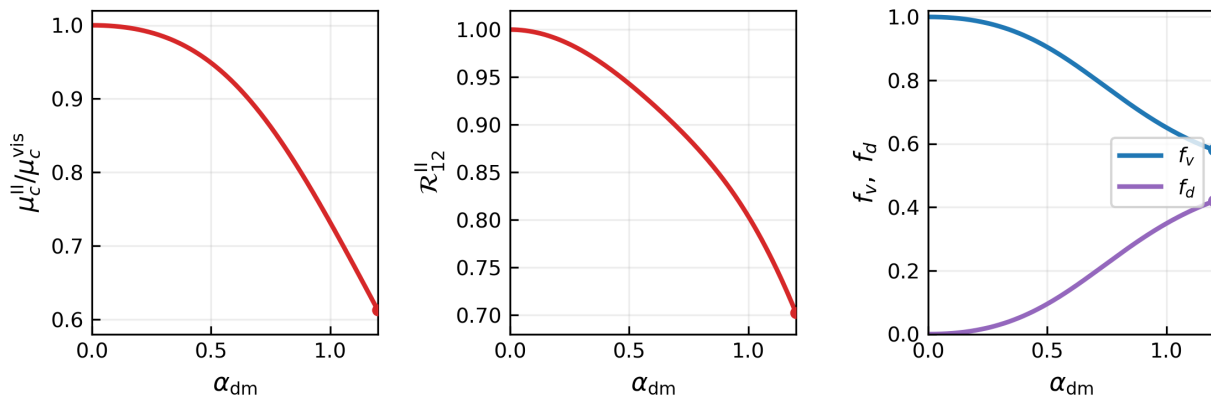


FIG. 3. Case-II visible–hidden hybridization in the minimal hidden-current ensemble. The left panel shows the coupled critical-scale ratio, the middle panel shows the entanglement-anisotropy stress factor, and the right panel shows the visible and hidden fractions of the critical vector mode. No  $(D, \theta, z, W)$  scan is plotted here because these three quantities are algebraic functions of  $\alpha_{\text{dm}}$ : the two vector channels share the same radial weight, so the scan collapses to the same curves. The all-case  $(\theta, z)$  comparison is shown in Fig. 2.

### V.B. Sourced scalar portal: width tomography instead of scalar hair

The scalar portal is treated as a sourced dark-sector deformation, not as a spontaneous scalar-hair phase. We solve the dilaton-dressed scalar BVP in Eqs. (II.79)–(II.80) and insert the resulting solution into the gauge-kinetic factor  $Z_{\text{dm}}(\Phi)$ . The representative Case-III-b scan uses  $\Delta_\Phi = 1.10$ , UV cutoff  $U = 80$ , reference width  $W = 0.10$ , and UV coefficient  $\Phi_{\text{src}} = 0.4$ , defined by  $\Phi(U) = \Phi_{\text{src}} U^{-\Delta_\Phi}$ . These values are chosen for three practical reasons. First,  $\Delta_\Phi = 1.10$  lies away from the two-falloff collision region, so the extracted width exponent is stable; Fig. 4 separately scans  $\Delta_\Phi$  to show that the exponent law is not tied to this value. Second,  $U = 80$  makes the sourced scalar solution insensitive to the UV cutoff over the displayed widths. Third,  $W = 0.10$  keeps the RT surface in the short-width regime where the short-width expansion in Eq. (IV.70) is reliable. The source amplitude  $\Phi_{\text{src}} = 0.4$  keeps the portal perturbative; changing it rescales the displayed Case-III-b magnitude as  $\Phi_{\text{src}}^2$ , while the sign, the separation between null/scale-independent/running channels, and the exponent are unchanged. For the sourced scalar solution, the slower UV falloff selected by the BVP controls the short-width portal response,

$$\frac{O_{12}^{\text{portal}}(W) - O_{12}^{\text{vis}}(W)}{|O_{12}^{\text{vis}}(W)|} \propto W^{2\Delta_{\text{UV}}}, \quad \Delta_{\text{UV}} = \min\{\Delta_\Phi, d(1+\theta) + z - \Delta_\Phi\}. \quad (\text{V.2})$$

Figure 4 verifies this exponent against the numerical scalar solutions. The HSV exponents matter here in the precise way expected from the UV radial equation: they enter  $d(1+\theta)+z$  and therefore can change the short-width power, but they do not change the fact that a scalar kinetic portal is the width-running channel while the hidden-current case is a constant channel. This is the safe level of scalar analysis for the present paper: it establishes a controlled susceptibility of the visible p-wave sector to a sourced dark scalar. A complete nonlinear scalar-hair phase diagram would require a source-free scalar condensate, scalar self-interactions, scalar stress tensor, and simultaneous Einstein–Yang–Mills–scalar backreaction; those ingredients are not claimed here.

The radial mechanism is shown in Fig. 5 in all three bulk dimensions. The figure is not restricted to a single  $D$  because the mechanism is geometric rather than tied to one analytic background: short regions remain close to the boundary, where the sourced scalar solution is small, while wider regions reach the radial domain where  $Z_{\text{dm}}(\Phi(u))$  reweights the Yang–Mills source. Varying  $D$ ,  $\theta$ , and  $z$  changes how quickly the RT surface moves through the radial direction, but the classification seen by the response remains the same. In  $D = 3$  this statement refers to the interval coefficient; in  $D = 4, 5$  it refers to the strip-orientation difference. The null cases remain at zero response in the orientation-difference rows, Case II is flat in  $W$ , and only Case III-b runs with width.

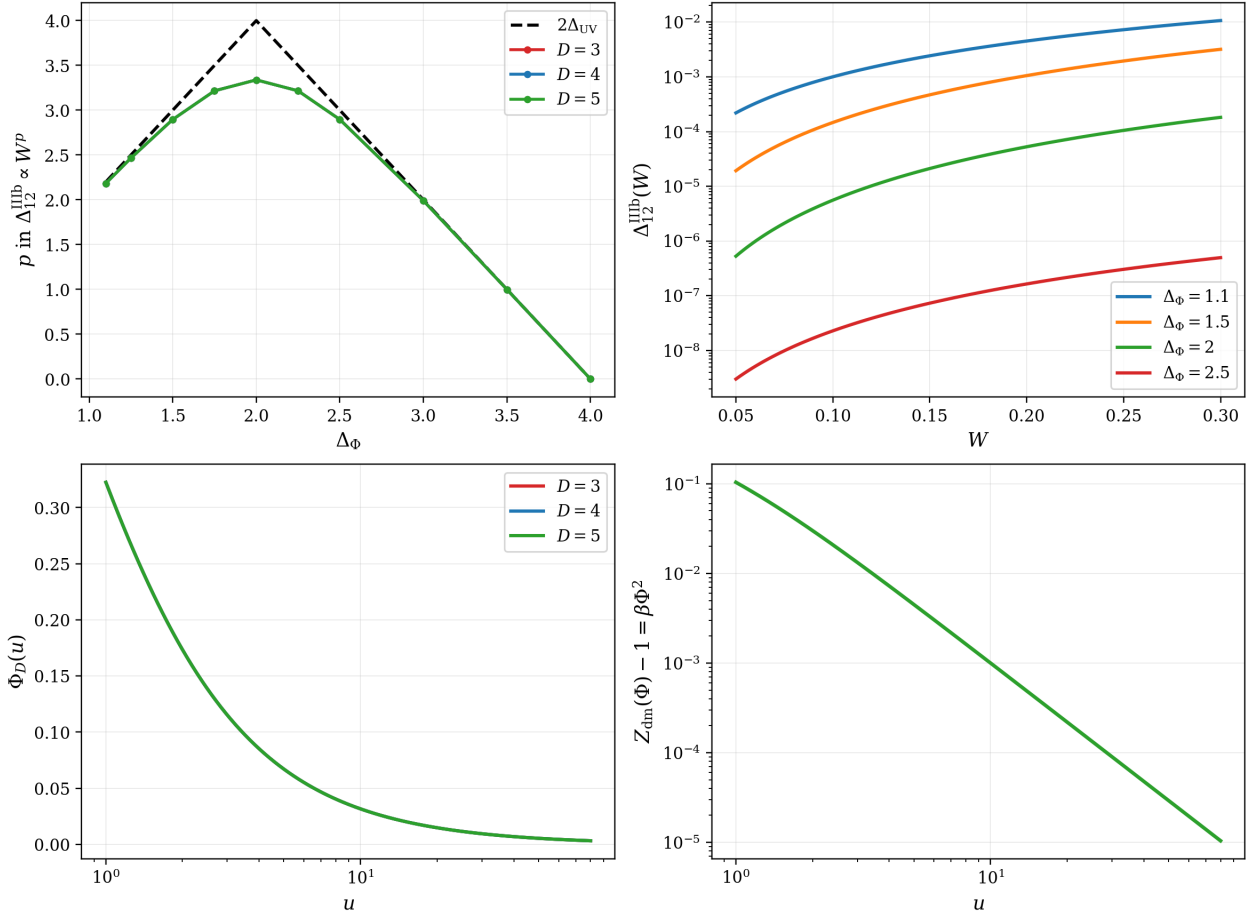


FIG. 4. Sourced scalar BVP and width exponent. The numerical exponent  $p$  is compared directly with twice the selected UV falloff. The upper-right panel shows the width dependence of the well-conditioned perturbative Case-III-b response. The lower panels show the corresponding scalar solution and kinetic factor. The mild undershoot near the two-falloff collision point is the expected degeneracy, not a change of the short-distance law.

### V.C. Finite-amplitude vector solutions and phase information

The linear zero-mode threshold must connect to a source-free ordered solution before it can be interpreted as a superfluid transition. Figure 6 therefore replaces the previous schematic normalized curve by a diagnostic from the nonlinear BVP solution tables. We use the figure as a numerical validation of the source-free vector solution and of the cutoff-stability of the grand-potential diagnostic. This restriction is deliberate. Case I and Case III-a do not generate a leading anisotropic source in  $O_{12}$ , while Case III-b is treated here as a sourced scalar susceptibility rather than as a complete source-free scalar-hair solution. A nonlinear ordered solution for the scalar portal would require the full Einstein–Yang–Mills–scalar system and is outside the present claim.

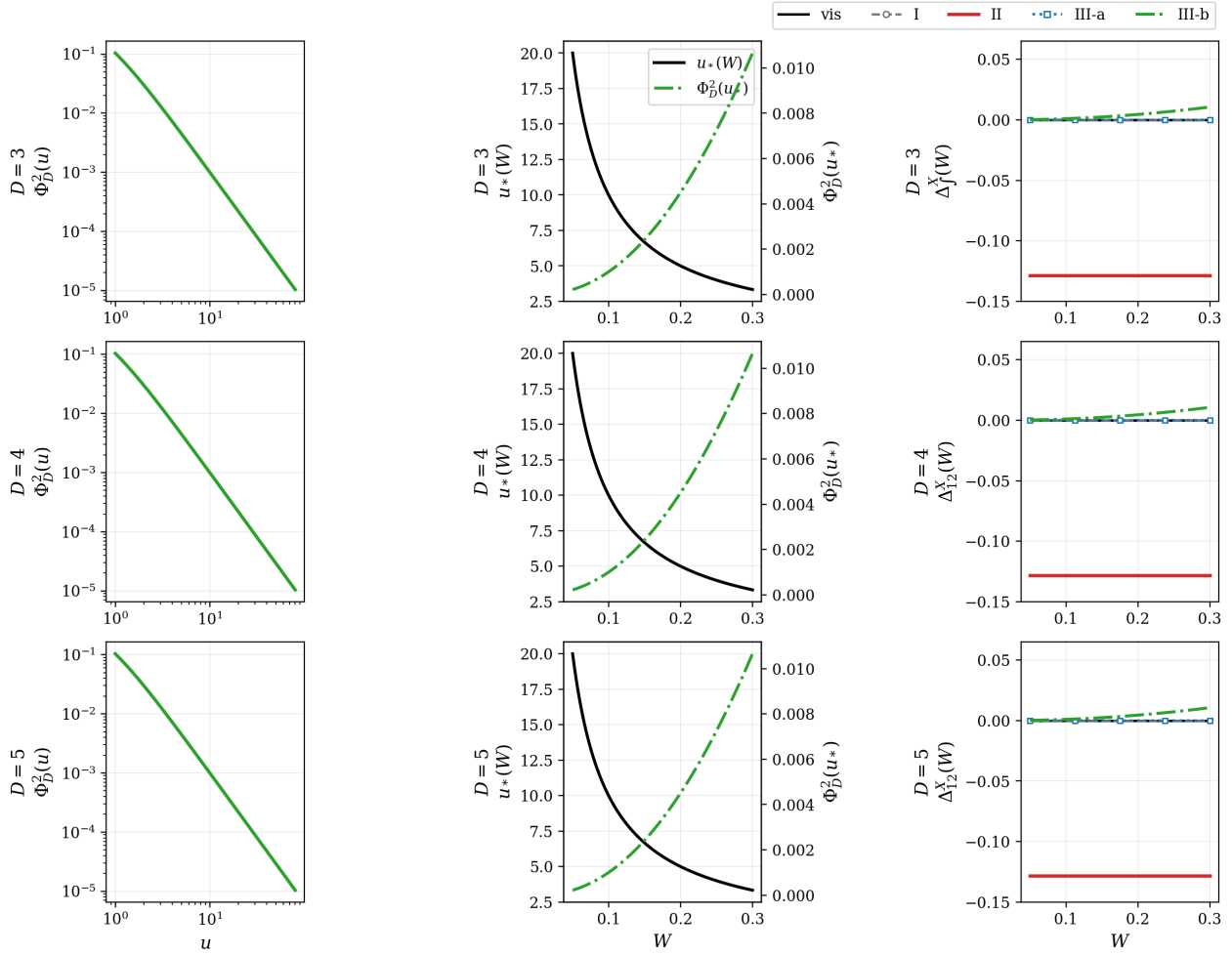


FIG. 5. Radial origin of the running response in  $D=3,4,5$ . The first column shows the sourced scalar solution squared. The second column displays the leading short-width scalar contribution together with the RT turning point, showing how wider regions reach deeper radial data. The third column compares the case responses: Case I and Case III-a sit on the null line, Case II is a  $W$ -independent hidden-current factor, and Case III-b is the running scalar-portal channel.

The finite-amplitude diagnostics are computed in the controlled hidden-current sector and are cross-checked against residual and cutoff tables. They should not be read as a global nonlinear phase diagram for every dark deformation. Their role is to verify that the critical mode used in the entanglement analysis is tied to a source-free ordered vector solution, while the scalar-portal figures separately establish only the sourced susceptibility and width exponent.

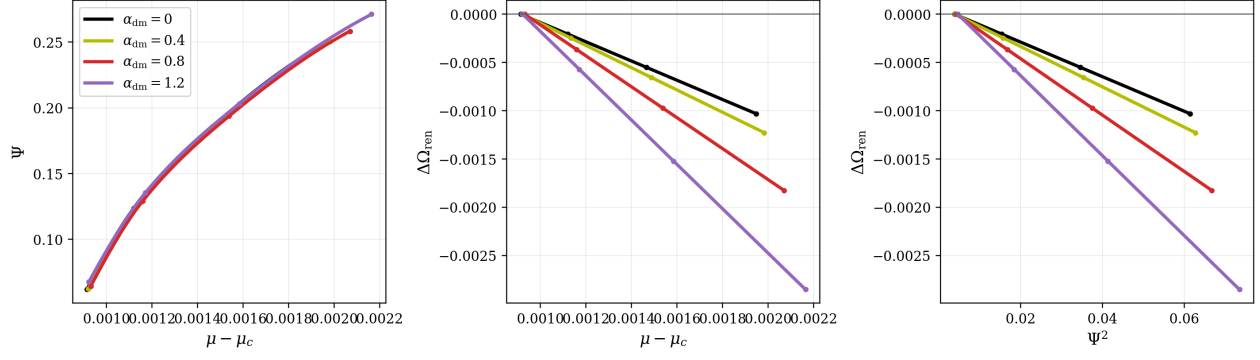


FIG. 6. Source-free vector-solution check from the nonlinear BVP table. The panels show the condensate amplitude, the ordered-state grand-potential difference, and the same difference as a function of the condensate squared. These curves validate the source-free vector solution used to interpret the critical zero-mode solution. They are not a full scalar-hair phase diagram for Case III-b.

## VI. DISCUSSION

*Boundary interpretation of the dark deformations.* The safest interpretation of our results is as a set of controlled current-sector deformations of an effective HSV boundary regime. The visible Abelian background fixes a finite-density state. The visible non-Abelian bulk field is dual to a flavor-current multiplet  $J_\mu^a$ , and the ordered solution is the vector-current condensate

$$\langle O \rangle \equiv \langle J_{x_1}^1 \rangle. \quad (\text{VI.1})$$

Thus the central question is not whether an abstract dark field changes a black-brane solution, but which boundary current channel it deforms and how that deformation is projected onto observable quantities. In this respect our use of entanglement anisotropy differs from the single visible-sector problem: the visible condensate supplies the direction and the reference  $O_{12}$ , while the hidden sector is diagnosed by whether it is filtered out, rescales that reference response, or produces a width-dependent correction.

For the hidden-gauge cases, the boundary deformation is naturally current-current rather than single-operator scalar. The schematic boundary expression we use is a generating functional for sources and responses, not an additional microscopic Lagrangian:

$$S_{\text{bdy}}^{\text{eff}}[A^{(0)}, C^{(0)}] = S_{\text{HSV}}^{\text{vis}}[A^{(0)}] + S_{\text{HSV}}^{\text{hid}}[C^{(0)}] + \frac{\alpha_{\text{dm}}}{2} \mathcal{N}_J \int dt d^d x \sqrt{-g_{(0)}} g_{(0)}^{\mu\nu} \delta_{ab} J_{\text{vis}\mu}^a J_{X\nu}^b + \dots \quad (\text{VI.2})$$

Here  $A_\mu^{(0)a}$  and  $C_\mu^{(0)a}$  are the visible and hidden boundary sources, and

$$J_{\text{vis}a}^\mu \equiv \frac{1}{\sqrt{-g_{(0)}}} \frac{\delta S_{\text{HSV}}^{\text{vis}}}{\delta A_\mu^{(0)a}}, \quad J_{Xa}^\mu \equiv \frac{1}{\sqrt{-g_{(0)}}} \frac{\delta S_{\text{HSV}}^{\text{hid}}}{\delta C_\mu^{(0)a}} \quad (\text{VI.3})$$

are the corresponding conserved-current responses. The constant  $\mathcal{N}_J$  absorbs the current normalization and engineering dimension, while  $\alpha_{\text{dm}}$  is the dimensionless bulk mixing parameter used in the radial equations. The boundary index  $\mu = 0, \dots, d$  runs over time and the  $d$  spatial directions,  $g_{(0)\mu\nu}$  is the boundary metric representative, and  $a, b$  are adjoint flavor indices for the hidden-SU(2) version of Case II. For Case I the hidden current is Abelian and the adjoint index on  $J_X$  is absent. The functionals  $S_{\text{HSV}}^{\text{vis/hid}}$  summarize connected current correlators of the two sectors in the effective HSV scaling regime. The dots denote local counterterms, higher-derivative terms and higher-current operators not included in the leading portal. With these definitions, Eq. (VI.2) simply encodes the off-diagonal source/response matrix implemented in the bulk by gauge kinetic mixing. When the hidden source is held fixed or set to zero, the hidden current sector can be eliminated, leaving an induced deformation of the visible current susceptibility. This is the origin of a scale-independent hidden-current factor in the minimal Case-II ensemble. In the coupled-mode treatment the factor is  $\mathcal{R}_{\text{HEE}}^{\text{II}} = 1 + \alpha_{\text{dm}}\gamma + \gamma^2$ .

From an RG perspective,  $\alpha_{\text{dm}}$  is a portal coupling of the effective current sector. If the HSV regime is embedded in a UV-complete theory, this coupling may have a beta function and can

trigger a flow of the current two-point matrix. We do not compute that UV beta function. Instead, the holographic calculation treats  $\alpha_{\text{dm}}$  as a parameter of the finite-density scaling regime and computes the radial flow of response functions within that regime. In Case II this radial flow is algebraic in the sense that the dark response is controlled by the coupled visible–hidden mixing ratio rather than by a new radial field. In Case III-b the scalar-dependent kinetic factor  $Z_{\text{dm}}(\Phi(u))$  makes the deformation genuinely radial and therefore radially dependent.

Cases III-a and III-b have a different boundary interpretation from hidden-gauge kinetic mixing, but they are still dark-sector deformations. They introduce an independent dark scalar operator  $\mathcal{O}_\Phi$ , neutral only with respect to the visible  $SU(2)$  flavor symmetry, and couple it to the visible current sector through  $\alpha_{\text{dm}}$ -controlled portal terms. Case III-a is an isotropic dark-scalar mass portal for the visible vector mode. Case III-b is a dark-scalar kinetic portal that makes the effective Yang–Mills kinetic operator depend on  $\Phi(u)$ . Boundary-wise, the scalar cases describe a dark scalar environment that can imitate, suppress, or enhance the visible vector-current instability without introducing a second hidden gauge current.

This distinction also explains why the figures are not redundant measurements of one number. The critical scale  $\mu_c$  answers the spectral question: which deformation first makes the normal vector-current operator marginally unstable? The radial-source panels then show where in the bulk the same critical eigenfunction deposits anisotropic stress. HEE performs a different projection of that stress: the RT surface weights the order- $\epsilon^2$  metric response according to the size and orientation of the boundary region. Finally, the condensate check asks whether the zero mode continues into a finite-amplitude source-free vector solution. A dark channel can therefore be prominent in  $\mu_c$  but nearly absent in the strip difference if its stress is isotropic, while a radial kinetic portal can leave  $\mu_c$  almost unchanged and still produce a width-dependent entanglement response. The apparent non-uniformity across figures is the point: each panel is a different projection of the same current-sector deformation.

*What the HSV scan shows.* The HSV geometry should not be read as the UV completion of a known microscopic Lagrangian. It is an effective scaling regime of a finite-density boundary theory with dynamical exponent  $z$  and hyperscaling-violation exponent  $\theta$ . In the present calculation its main role is to vary the radial weights of the same visible p-wave system. This lets us check whether the hidden-sector separation is an accident of one background or a feature of the current-sector tensor structure. The outcome is that the latter controls the qualitative result. Purely temporal or isotropic hidden sectors do not source the traceless spatial Einstein equation, so they drop out of the strip orientation difference. Hidden  $SU(2)$  mixing preserves the visible radial weight and gives an  $\alpha_{\text{dm}}$ -dependent but  $W$ -independent factor. The scalar gauge-kinetic portal is different because it inserts a radially varying function into the Yang–Mills operator. Changing  $\theta$  and  $z$  changes the radial weights, the visible normalization, and the UV scalar falloff, but it does not change this hierarchy of mechanisms.

This is how the HSV survey should be read. It is not evidence that the null, scale-independent, and width-running channels exist only at special HSV parameters. Rather, the

survey shows that the entanglement classification is universal within the family of scaling backgrounds considered here, with geometry-dependent changes appearing mainly in amplitudes, RT weights, and the scalar short-width exponent. The hidden- $SU(2)$  case is the limiting case in which the common radial weight makes the answer algebraic, while the scalar kinetic portal is the case in which the radial weight is genuinely deformed.

*Physical reading in different dimensions.* The  $D = 3$  figures should be interpreted as interval probes of the total metric response. Since there is no independent transverse strip orientation, the interval coefficient  $\Delta S_{\text{int}}^{(2)}$  does not enforce the same isotropic-sector null rule as  $\mathcal{O}_{12}^{(2)}$  in higher dimensions. Thus a hidden charge-sector deformation can remain visible in  $D = 3$  even when its higher-dimensional strip-anisotropy counterpart is null. This makes  $D = 3$  a useful check of the full response chain, but not the sharpest check of directional anisotropy.

The  $D = 4$  and  $D = 5$  HEE figures are sharper because they use the signed orientation difference

$$\mathcal{O}_{12}^{(2)} = S_{\perp}^{(2)} - S_{\parallel}^{(2)}. \quad (\text{VI.4})$$

This observable is designed to subtract the isotropic part of the RT response. Therefore Case I and Case III-a are not expected to produce a leading signal unless they generate an anisotropic stress component. Their near-coincidence with the visible curve is not a numerical failure; it is a selection rule of the observable. Case II is visible because it rescales the vector stress by an algebraic hidden-current factor and because the critical vector mode has a genuine hidden component. Case III-b is visible because it changes the radial kinetic matrix and therefore the source solution feeding the metric perturbation. The mild dependence on  $\theta$  and  $z$  in the relative strip rows should be read in this light: the exponents change how the same mechanism is weighted along the radial direction, while the separation of the mechanisms themselves persists.

The ordered-solution diagnostics add a complementary statement. They verify that the zero-mode critical point corresponds to a source-free ordered solution and not merely to a linearized eigenvalue. In the Case-II curves, the hidden sector lowers the chemical potential needed to form  $\langle J_{x_1}^1 \rangle$ ; at fixed visible normalization this appears as a leftward displacement of the condensate curve. We use these curves to support the critical-point interpretation, not to claim a full global nonlinear phase diagram for every dark deformation.

*Scalar-sector scope.* The scalar analysis in this paper is deliberately limited to a sourced dark-scalar portal. This is sufficient for the scale-resolved diagnostic because the question is how a prescribed hidden radial operator deforms the visible p-wave current sector. It is not a claim that the dark scalar itself condenses spontaneously. A complete nonlinear scalar-hair phase diagram would require solving the source-free scalar problem, including a self-interacting potential, the scalar stress tensor, and the simultaneous backreaction of  $\Phi$ ,  $B_M^a$ , and the metric. The present calculation therefore proves a controlled portal susceptibility and a width-exponent law, not a new scalar-hair phase.

*Limitations and future works.* The HSV geometries used here are effective finite-density scaling backgrounds rather than unique UV-complete boundary Lagrangians. The conclusions

should therefore be read as statements about hidden-sector deformations of the current sector within such scaling regimes. The log-violating HSS regime lies in the opposite sign convention for the hyperscaling exponent and is outside the non-negative  $\theta$  scan used in this work.

The hidden-sector cases also have different microscopic status. Cases I and II are hidden gauge sectors with specified residual gauge symmetry. Case I is interpreted after selecting the color-3 Abelian embedding of the normal phase. Case II is invariant under the diagonal subgroup of  $SU(2)_{\text{vis}} \times SU(2)_{\text{hid}}$ . Cases III-a and III-b are hidden scalar portal models; the scalar is a singlet outside the visible p-wave multiplet and communicates with it only through the portal couplings.

The coupled hidden-current model is exact only for the minimal Case-II ensemble used in Sec. III.C 2a. It is not a universal law for arbitrary hidden sources. Finally, the scalar-portal results are linear-response statements for a sourced dark scalar. Promoting them to a fully backreacted scalar-hair phase diagram is a separate problem.

## Appendix A: RT normalization checks

The main text keeps only the six figures that support the scale-resolved hidden-sector interpretation. We nevertheless retain the small-subsystem first-law checks because they fix the normalization of the RT first variation used throughout the paper. The check compares the leading change of the interval or strip entropy with the corresponding boundary energy variation,  $\Delta S = \Delta E/T_{\text{ent}}$ , for the visible anisotropic solution. Once this normalization is fixed, the dark-sector cases are interpreted by their stress sources rather than by changing the RT prescription itself: Case I and Case III-a remain null in the strip-orientation difference when their stress is isotropic, Case II rescales the same anisotropic source by the coupled-current factor, and Case III-b changes the radial weight that the RT kernel averages. Thus the appendix supports the normalization and interpretation of the main figures without adding an independent dark-sector phase claim.

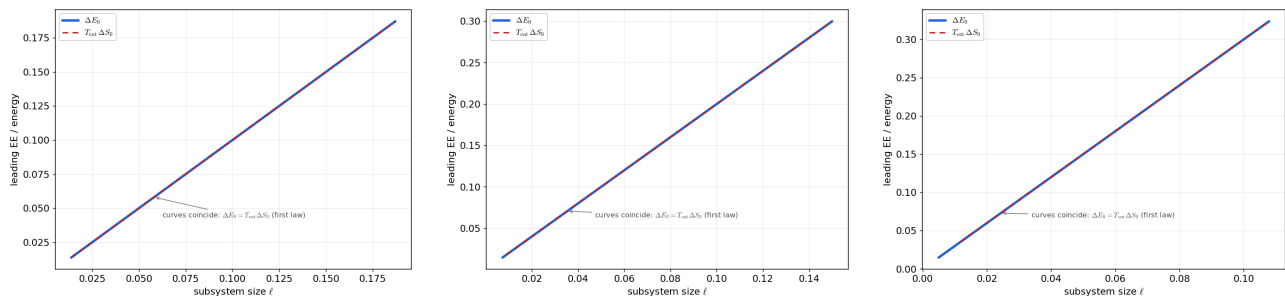


FIG. 7. RT normalization checks for the small-subsystem first law. The left panel is the  $D = 3$  interval check, the middle panel is the  $D = 4$  strip check, and the right panel is the  $D = 5$  strip check. These plots validate the normalization of the leading RT response and do not introduce an additional dark-sector channel.

## NUMERICAL METHODS AND DATA AVAILABILITY

All Sturm–Liouville, coupled-mode, metric-response, and RT first-variation data used in the figures are generated by the companion numerical scripts and CSV tables supplied with the following github repository: [https://github.com/jiseongchae17hepth/Dark\\_sector\\_deformations\\_of\\_anisotropic\\_holographic\\_superfluid\\_in\\_hyperscaling\\_violation\\_geometry.git](https://github.com/jiseongchae17hepth/Dark_sector_deformations_of_anisotropic_holographic_superfluid_in_hyperscaling_violation_geometry.git)

---

- [1] J. M. Maldacena, “The Large N limit of superconformal field theories and supergravity,” *Adv. Theor. Math. Phys.* **2** (1998) 231 [hep-th/9711200].
- [2] S. S. Gubser, I. R. Klebanov and A. M. Polyakov, “Gauge theory correlators from non-critical string theory,” *Phys. Lett. B* **428** (1998) 105 [hep-th/9802109].
- [3] E. Witten, “Anti-de Sitter space and holography,” *Adv. Theor. Math. Phys.* **2** (1998) 253 [hep-th/9802150].
- [4] O. Aharony, S. S. Gubser, J. M. Maldacena, H. Ooguri and Y. Oz, “Large N field theories, string theory and gravity,” *Phys. Rept.* **323** (2000) 183 [hep-th/9905111].
- [5] D. T. Son and A. O. Starinets, “Minkowski-space correlators in AdS/CFT correspondence,” *JHEP* **09** (2002) 042 [hep-th/0205051].
- [6] N. Iqbal and H. Liu, “Universality of the hydrodynamic limit in AdS/CFT and the membrane paradigm,” *Phys. Rev. D* **79** (2009) 025023 [arXiv:0809.3808].
- [7] G. Policastro, D. T. Son and A. O. Starinets, “The shear viscosity of strongly coupled N=4 supersymmetric Yang–Mills plasma,” *Phys. Rev. Lett.* **87** (2001) 081601 [hep-th/0104066].
- [8] G. Policastro, D. T. Son and A. O. Starinets, “From AdS/CFT correspondence to hydrodynamics,” *JHEP* **09** (2002) 043 [hep-th/0205052].
- [9] P. Kovtun, D. T. Son and A. O. Starinets, “Viscosity in strongly interacting quantum field theories from black hole physics,” *Phys. Rev. Lett.* **94** (2005) 111601 [hep-th/0405231].
- [10] S. Bhattacharyya, V. E. Hubeny, S. Minwalla and M. Rangamani, “Nonlinear fluid dynamics from gravity,” *JHEP* **02** (2008) 045 [arXiv:0712.2456].
- [11] S. Bhattacharyya, R. Loganayagam, S. Minwalla, S. Nampuri, S. P. Trivedi and S. R. Wadia, “Forced fluid dynamics from gravity,” *JHEP* **02** (2009) 018 [arXiv:0806.0006].
- [12] S. S. Gubser and S. S. Pufu, “The gravity dual of a p-wave superconductor,” *JHEP* **11** (2008) 033 [arXiv:0805.2960].
- [13] M. M. Roberts and S. A. Hartnoll, “Pseudogap and time reversal breaking in a holographic superconductor,” *JHEP* **08** (2008) 035 [arXiv:0805.3898].
- [14] J. Erdmenger, P. Kerner and H. Zeller, “Non-universal shear viscosity from Einstein gravity,” *Phys. Lett. B* **699** (2011) 301 [arXiv:1011.5912].

- [15] P. Basu and J. H. Oh, “Analytic approaches to anisotropic holographic superfluids,” *JHEP* **07** (2012) 106 [arXiv:1109.4592].
- [16] J. H. Oh, “Running shear viscosities in anisotropic holographic superfluids,” *JHEP* **06** (2012) 103 [arXiv:1201.5605].
- [17] B. Holdom, “Two U(1)’s and epsilon charge shifts,” *Phys. Lett. B* **166** (1986) 196.
- [18] K. R. Dienes, C. F. Kolda and J. March-Russell, “Kinetic mixing and the supersymmetric gauge hierarchy,” *Nucl. Phys. B* **492** (1997) 104 [hep-ph/9610479].
- [19] S. A. Abel and B. W. Schofield, “Brane-antibrane kinetic mixing, millicharged particles and SUSY breaking,” *Nucl. Phys. B* **685** (2004) 150 [hep-th/0311051].
- [20] S. A. Abel, J. Jaeckel, V. V. Khoze and A. Ringwald, “Illuminating the hidden sector of string theory by shining light through a magnetic field,” *Phys. Lett. B* **666** (2008) 66 [hep-ph/0608248].
- [21] S. A. Abel, M. D. Goodsell, J. Jaeckel, V. V. Khoze and A. Ringwald, “Kinetic mixing of the photon with hidden U(1)s in string phenomenology,” *JHEP* **07** (2008) 124 [arXiv:0803.1449].
- [22] L. Nakonieczny and M. Rogatko, “Analytic study on backreacting holographic superconductors with dark matter sector,” *Phys. Rev. D* **90** (2014) 106004 [arXiv:1411.0798].
- [23] L. Nakonieczny, M. Rogatko and K. I. Wysokiński, “Magnetic field in holographic superconductors with dark matter sector,” *Phys. Rev. D* **91** (2015) 046007 [arXiv:1501.04902].
- [24] L. Nakonieczny, M. Rogatko and K. I. Wysokiński, “Analytic investigation of holographic phase transitions influenced by dark matter sector,” *Phys. Rev. D* **92** (2015) 066008 [arXiv:1509.01769].
- [25] M. Rogatko and K. I. Wysokiński, “P-wave holographic superconductor/insulator phase transitions affected by dark matter sector,” *JHEP* **03** (2016) 215 [arXiv:1508.02869].
- [26] M. Rogatko and K. I. Wysokiński, “Holographic vortices in the presence of dark matter sector,” *JHEP* **12** (2015) 041 [arXiv:1510.06137].
- [27] M. Rogatko and K. I. Wysokiński, “Condensate flow in holographic models in the presence of dark matter,” *JHEP* **10** (2016) 152 [arXiv:1608.00343].
- [28] Y. Peng, “Holographic entanglement entropy in superconductor phase transition with dark matter sector,” *Phys. Lett. B* **750** (2015) 420 [arXiv:1507.07399].
- [29] Y. Peng, Q. Pan and Y. Liu, “A general holographic insulator/superconductor model with dark matter sector away from the probe limit,” *Nucl. Phys. B* **915** (2017) 69 [arXiv:1512.08950].
- [30] C. Park, G. Kim, J. s. Chae and J. H. Oh, *JHEP* **02**, 182 (2023) doi:10.1007/JHEP02(2023)182 [arXiv:2210.08919 [hep-th]].
- [31] B. Kiczek, M. Rogatko and K. I. Wysokiński, “Holographic DC SQUID in the presence of dark matter,” arXiv:1904.00653.
- [32] M. Rogatko and K. I. Wysokiński, “Two interacting current model of holographic Dirac fluid in graphene,” *Phys. Rev. D* **97** (2018) 024053 [arXiv:1708.08051].
- [33] M. Rogatko and K. I. Wysokiński, “Holographic calculation of magneto-transport coefficients in Dirac semimetals,” *JHEP* **01** (2018) 078 [arXiv:1710.05002].

- [34] M. Rogatko and K. I. Wysokiński, “Viscosity bound for anisotropic superfluids with dark matter sector,” *Phys. Rev. D* **96** (2017) 026015 [arXiv:1612.02593].
- [35] X. Dong, S. Harrison, S. Kachru, G. Torroba and H. Wang, “Aspects of holography for theories with hyperscaling violation,” *JHEP* **06** (2012) 041 [arXiv:1201.1905].
- [36] B. Goutéraux and E. Kiritsis, “Generalized holographic quantum criticality at finite density,” *JHEP* **12** (2011) 036 [arXiv:1107.2116].
- [37] L. Huijse, S. Sachdev and B. Swingle, “Hidden Fermi surfaces in compressible states of gauge-gravity duality,” *Phys. Rev. B* **85** (2012) 035121 [arXiv:1112.0573].
- [38] M. Alishahiha, E. O. Colgain and H. Yavartanoo, “Charged Black Branes with Hyperscaling Violating Factor,” *JHEP* **11** (2012) 137 [arXiv:1209.3946].
- [39] G. Kim, Y. S. Choi and J. H. Oh, “Analytic approaches to anisotropic holographic superfluids in asymptotically hyperscaling violation geometry,” arXiv:2504.13635.
- [40] H.-S. Jeong, W.-B. Pan, Y.-W. Sun and Y.-T. Wang, “Holographic study of  $T\bar{T}$  like deformed HV QFTs: holographic entanglement entropy,” *JHEP* **02** (2023) 018 [arXiv:2211.00518].
- [41] G. Cavini, D. Seminara, J. Sisti and E. Tonni, “On shape dependence of holographic entanglement entropy in  $AdS_4/CFT_3$  with Lifshitz scaling and hyperscaling violation,” *JHEP* **02** (2020) 172 [arXiv:1907.10030].
- [42] C. Ran, S.-F. Wu and Z.-Y. Xian, “Learning geometries beyond asymptotic AdS,” *JHEP* **03** (2026) 031 [arXiv:2508.05808].
- [43] S. Ryu and T. Takayanagi, “Holographic derivation of entanglement entropy from AdS/CFT,” *Phys. Rev. Lett.* **96** (2006) 181602 [hep-th/0603001].
- [44] S. Ryu and T. Takayanagi, “Aspects of holographic entanglement entropy,” *JHEP* **08** (2006) 045 [hep-th/0605073].
- [45] S. N. Solodukhin, “Entanglement entropy, conformal invariance and extrinsic geometry,” *Phys. Lett. B* **665** (2008) 305 [arXiv:0802.3117].
- [46] L.-Y. Hung, R. C. Myers and M. Smolkin, “On holographic entanglement entropy and higher curvature gravity,” *JHEP* **04** (2011) 025 [arXiv:1101.5813].
- [47] H. Casini, M. Huerta and R. C. Myers, “Towards a derivation of holographic entanglement entropy,” *JHEP* **05** (2011) 036 [arXiv:1102.0440].
- [48] J. Bhattacharya, M. Nozaki, T. Takayanagi and T. Ugajin, “Thermodynamical property of entanglement entropy for excited states,” *Phys. Rev. Lett.* **110** (2013) 091602 [arXiv:1212.1164].
- [49] E. Bianchi and R. C. Myers, “On the architecture of spacetime geometry,” *Class. Quant. Grav.* **31** (2014) 214002 [arXiv:1212.5183].
- [50] M. Nozaki, T. Numasawa, A. Prudenziati and T. Takayanagi, “Dynamics of entanglement entropy from Einstein equation,” *Phys. Rev. D* **88** (2013) 026012 [arXiv:1304.7100].
- [51] V. Rosenhaus and M. Smolkin, “Entanglement entropy: a perturbative calculation,” *JHEP* **12** (2014) 179 [arXiv:1403.3733].

- [52] V. Rosenhaus and M. Smolkin, “Entanglement entropy, planar surfaces, and spectral functions,” *JHEP* **02** (2015) 015 [arXiv:1410.6530].
- [53] S. S. Gubser, “Colorful horizons with charge,” *Phys. Rev. Lett.* **101** (2008) 191601 [arXiv:0803.3483].
- [54] S. A. Hartnoll, C. P. Herzog and G. T. Horowitz, “Building a holographic superconductor,” *Phys. Rev. Lett.* **101** (2008) 031601 [arXiv:0803.3295].
- [55] S. A. Hartnoll, C. P. Herzog and G. T. Horowitz, “Holographic superconductors,” *JHEP* **12** (2008) 015 [arXiv:0810.1563].
- [56] C. P. Herzog, “Lectures on holographic superfluidity and superconductivity,” *J. Phys. A* **42** (2009) 343001 [arXiv:0904.1975].
- [57] G. T. Horowitz, “Introduction to holographic superconductors,” *Lect. Notes Phys.* **828** (2011) 313 [arXiv:1002.1722].
- [58] M. Park, J. Park and J. H. Oh, “Phase transition in anisotropic holographic superfluids with arbitrary  $z$  and  $\alpha$ ,” *Eur. Phys. J. C* **77** (2017) 810 [arXiv:1609.08241].
- [59] M. Ammon, J. Erdmenger, M. Kaminski and P. Kerner, “Superconductivity from gauge/gravity duality with flavor,” *Phys. Lett. B* **680** (2009) 516 [arXiv:0810.2316].
- [60] Z.-Y. Nie, R.-G. Cai, X. Gao and H. Zhang, “Competition between the s-wave and p-wave superconductivity phases in a holographic model,” *JHEP* **11** (2013) 087 [arXiv:1309.2204].
- [61] T. Nishida, “Phase diagram of a holographic superconductor model with s-wave and p-wave,” *JHEP* **09** (2014) 154 [arXiv:1403.6070].
- [62] W. Li, “Competition between s-wave order and p-wave order in holographic superconductors,” *JHEP* **11** (2014) 147 [arXiv:1405.0382].
- [63] R.-G. Cai, L. Li, L.-F. Li and R.-Q. Yang, “Introduction to holographic superconductor models,” *Sci. China Phys. Mech. Astron.* **58** (2015) 060401 [arXiv:1502.00437].
- [64] M. Ammon, J. Erdmenger, V. Grass, P. Kerner and A. O’Bannon, “On holographic p-wave superfluids with back-reaction,” *Phys. Lett. B* **686** (2010) 192 [arXiv:0912.3515].
- [65] J. Erdmenger, V. Grass, P. Kerner and T. H. Ngo, “Holographic superfluidity in imbalanced mixtures,” *JHEP* **08** (2011) 037 [arXiv:1103.4145].
- [66] S. A. Hartnoll, “Lectures on holographic methods for condensed matter physics,” *Class. Quant. Grav.* **26** (2009) 224002 [arXiv:0903.3246].
- [67] J. McGreevy, “Holographic duality with a view toward many-body physics,” *Adv. High Energy Phys.* **2010** (2010) 723105 [arXiv:0909.0518].
- [68] C. Charmousis, B. Gouteraux, B. S. Kim, E. Kiritsis and R. Meyer, “Effective holographic theories for low-temperature condensed matter systems,” *JHEP* **11** (2010) 151 [arXiv:1005.4690].
- [69] B. Gouteraux and E. Kiritsis, “Quantum critical lines in holographic phases with (un)broken symmetry,” *JHEP* **04** (2013) 053 [arXiv:1212.2625].
- [70] E. Kiritsis and J. Ren, “On holographic insulators and supersolids,” *JHEP* **09** (2015) 168 [arXiv:1503.03481].

- [71] S. Kachru, X. Liu and M. Mulligan, “Gravity duals of Lifshitz-like fixed points,” *Phys. Rev. D* **78** (2008) 106005 [arXiv:0808.1725].
- [72] M. Taylor, “Non-relativistic holography,” arXiv:0812.0530.
- [73] S. Bhattacharyya, S. Minwalla and K. Papadodimas, “Small hairy black holes in global AdS spacetime,” *JHEP* **11** (2011) 035 [arXiv:1005.1287].
- [74] P. Basu, J. He, A. Mukherjee and H.-H. Shieh, “Superconductivity from D3/D7: holographic pion superfluid,” *JHEP* **11** (2009) 070 [arXiv:0810.3970].
- [75] D. Mateos and D. Trancanelli, “The anisotropic N=4 super Yang–Mills plasma and its instabilities,” *Phys. Rev. Lett.* **107** (2011) 101601 [arXiv:1105.3472].
- [76] A. Rebhan and D. Steineder, “Violation of the holographic viscosity bound in a strongly coupled anisotropic plasma,” *Phys. Rev. Lett.* **108** (2012) 021601 [arXiv:1110.6825].